MASTER

Modelling of the Oxidative Coupling of Methane in Dense membrane reactor and Solid Oxide Fuel Cell

van der Weerd, H.C.N.

Award date:
2021

Department of Chemical Engineering
Sustainable Process Engineering -
Inorganic Membranes & Membrane Reactors

Modelling of the Oxidative Coupling of Methane in Dense membrane reactor and Solid Oxide Fuel Cell

Master Thesis

Hendrik van der Weerd

Committee:

Prof. Dr. Eng. F. Gallucci
Dr. Ir. M.F. Neira d'Angelo
Dr. Ing. H.R. Godini
Ir. A. Cruellas Labella

Eindhoven, June 2020

Abstract

Oxidative coupling of methane would be a desirable way of producing ethylene, were it not for a conversion-selectivity trade-off causing low yield. Distributed feeding of oxygen is a way of improving OCM performance compared to co-feeding. In this thesis a 2D reactor model is developed to investigate oxidative coupling of methane. Co-feeding and distributed-feeding reactor concepts are compared. Furthermore, power generation through the use of solid oxide fuel cell technology is investigated: the effluent of an OCM reactor (after product separation) can be effectively reformed within such a fuel cell and used for power generation. The two units can also be combined, by performing oxidative coupling of methane within a fuel cell in lieu of reforming. This does not lead to significant power generation, due to a thermodynamic limitation.

Contents

1 Introduction

Ethylene is a globally produced petrochemical of importance, with a number of important derivatives. For example, it is used in the manufacture of polyethylene, ethylene dichloride, ethylene oxide, ethyl benzene, and vinyl acetate, which are themselves platform chemicals with many products [1]. Ethylene production is even increasing, with new shale gas resources (mostly ethane) causing increased interest in steam cracking, partially leading to the replacement of naphta crackers, as shale gas is cheaper [2]. Besides shale gas, there has been a sustained interest for the valorization of methane over the last four decades, due to the low cost of methane [3]. Such interest has led to the development of the process known as Oxidative Coupling of Methane (OCM):

$$2CH_4 + O_2 \rightarrow C_2H_4 + 2H_2O \tag{1.1}$$

However, this reaction faces some important problems: First, the contacting of methane and oxygen must be done in such a way that explosive mixtures are avoided. Second, reasonable catalytic activity is only achieved at high temperatures in the neighbourhood of $800°C$, leading to the need for more expensive materials, and the reactor design is complicated by the strongly exothermic nature of the process. But most importantly, the yield for this reaction is always rather limited (in the range of 20% - 30%) [4]. The reason is of course that oxygen will gladly oxidize the hydrocarbons and form carbon oxides CO_x ('deep oxidation').

A number of approaches are being researched in order to increase the yield, including development of new catalysts, the use of alternative 'soft' oxidants, and different reactor engineering solutions. As can be seen in figure 1.1, some researchers have been able to surpass 30% yield (denoted by the upper curved line), but no one has been able to reach the 'techno-economic target area': this is a target minimum performance of 90% selectivity and 30% conversion, published in 1989 for a process using pure methane and air [5]. Process viability can only be determined by techno-economic assessment, but this target is assumed to still have some general applicability to all OCM processes. Additionally, it can be seen that the target minimum performance heavily favors selectivity; there are other researchers who came to the same conclusion [6, 7].

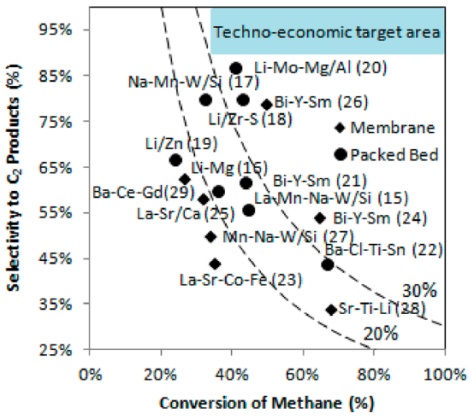

Figure 1.1: Various catalysts have been tested (all catalysts are oxides, but oxygen is omitted from the formulas to save space). Source: [4]

Numerous researchers have also looked towards novel reactor concepts in their efforts to improve reaction performance. Figure 1.2 shows selectivity versus conversion data obtained using different reactor concepts, along with a solid line denoting $S = 1 - X$. This line is a mathematical expression for the core challenge of OCM: it is hard to simultaneously have high conversion and high selectivity. The most interesting reactor concepts should be those which lie above this line.

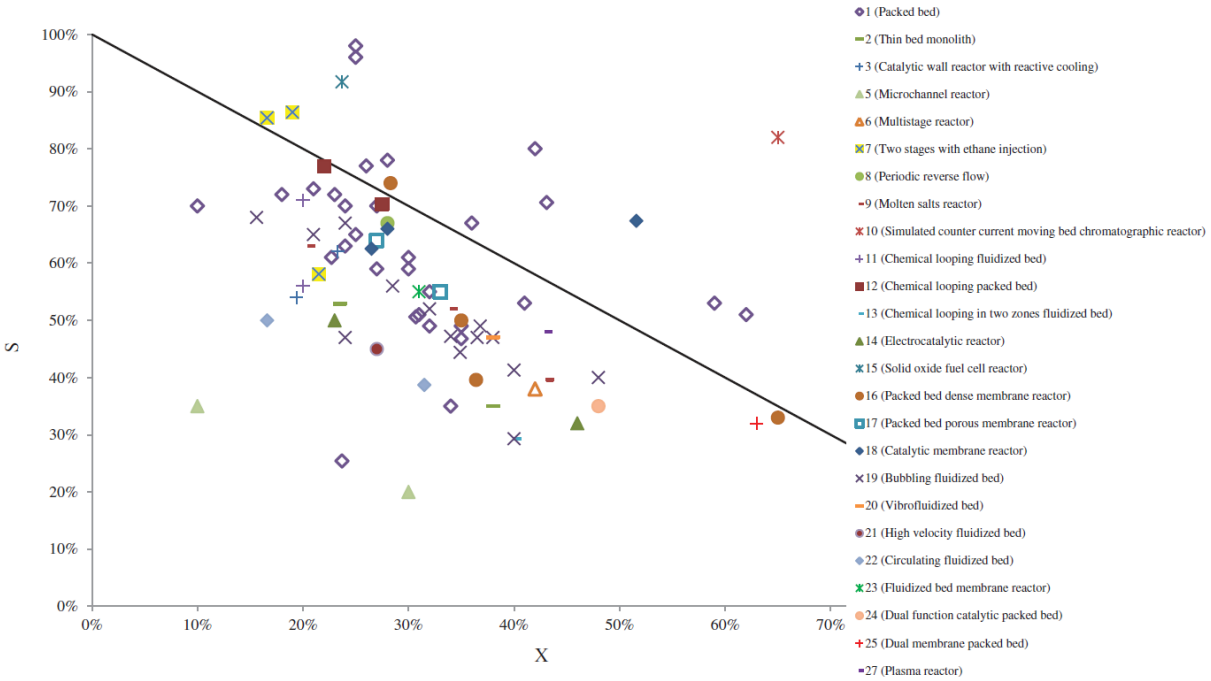

Figure 1.2: Numerous reactor concepts have been researched. Source: [8]

Interestingly, some of the very best results have been achieved in packed beds (the least novel reactor type). It is however important to note that these results have been obtained using the Lithium catalyst, which does not possess sufficient long term stability. Moreover, these experiments were preformed under high feed dilution, which is not desirable for an industrial process. Of the results presented in figure 1.2, the single best yield is obtained with a simulated counter current moving bed reactor concept. This reactor configuration consists of many units (a combination of reactors, separators, and heat management systems), which makes it more like an entire plant unto itself. The yield which is reported for this configuration ($> 50\%$) is not so exceptional when compared to any other reactor type combined with product separation and methane recycle. Another concept is the two-stages with ethane injection concept, which relies on operating the second stage at $520°C$, a temperature at which no known OCM catalyst is active (enough).

This leaves three promising concepts which happen to be very similar because of the distributed oxygen feeding policy: the dense membrane packed bed reactor, catalytic membrane reactor, and solid oxide fuel cell reactor. These reactors have a relatively good selectivity, due to the low oxygen concentration all along the reactor. This is discussed in more detail in section 2.1. But the selective feeding of oxygen also means that no external O_2/N_2 separation unit is needed. One important drawback that must be mentioned, is that these reactor concepts with a regulated low oxygen concentration will have relatively lower reaction rates, and therefore need larger reactor volumes. In terms of cost, the above has a couple of implications: First there are no costs for a separate air separation unit; but this amounts to only 5% - 10% of the total plant capital cost [6], and the reactor will be more expensive when using materials such as perovskites. Second, a higher selectivity means less carbon oxides need to be converted back into methane in the methanizer (CO_x hydrogenation), which can make up around a quarter of the capital cost [6]. So far, SOFC technology has been regarded as similar to the (dense) membrane reactors, but the defining feature is of course that power can be generated additionally. Given that around a quarter of the total price of OCM-generated ethylene is the cost of electricity [6], this could potentially make a big difference. However, that depends on wattage produced relative to rate of ethylene production.
In this thesis, the reactor-engineering aspect of OCM is investigated. Specifically, a packed bed configuration is first established to be improved upon. Then, a membrane configuration is adapted from it. Two SOFC concepts are to be compared: one in which power generation is integrated with OCM, and another in which the power generation is separated: OCM proceeds in the membrane reactor, and an internal reforming fuel cell is fed its effluent after separation of the C_2 products. In this way, power generation and the OCM reaction are made independent, allowing them to be separately operated.
In order to compare these different cases, a techno-economic analysis is needed. Although this is beyond the scope of this thesis, a simple estimation will be presented. The investigations of these various types of reactor are performed using a numerical model, as that provides the needed flexibility (as well as being safe and cheap). A 2D cylindrical strategy is adopted, as there is a significant need to resolve radial profiles of heat and mass in order to obtain more accurate results [9]. Porous membranes are disregarded, because of their decreased similarity with fuel cells in terms of reactor behaviour and plant design. Also, electrolytic cells (cells where power is provided to increase the oxygen flux) are beyond the scope. If the results indicate that the power-to-ethylene ratio is low in OCM-integrated fuel cells, that might warrant further investigation of electrolytic cells, as they are expected to exhibit higher capacity.

2 Theory

In this section a description will be given of relevant theoretical aspects of this work. First oxidative coupling of methane is discussed, followed by membranes for oxygen separation. The theory relevant to a solid oxide fuel cell is discussed, and finally the (dry) reforming reaction.

2.1 Oxidative Coupling of Methane

Conceptually, coupling of methane to produce ethylene is simple:

$$2CH_4 \rightarrow C_2H_4 + 2H_2$$

This is economically interesting because of the big difference in value between reactant and product, because of the great availability of methane and the high demand for ethylene. This reaction has been achieved, but suffers from rapid coking and an endothermicity which is even greater than that of steam cracking [3]. In order to overcome these problems, methane coupling can also be done in an oxidative manner:

$$2CH_4 + O_2 \rightarrow C_2H_4 + 2H_2O$$

Although clearly this leads to a new problem: oxidation to CO and CO_2. This leads to product loss and safety issues. OCM is characterized by a relatively complex set of parallel and consecutive reactions, and the need for high temperature (800°C) to activate the catalyst. The kinetic model published by Stansch et al. [10] has become one of the most widely accepted kinetic models [3]. The reaction steps which have been developed there, are also used in other kinetic models [11]. All

	OCM Reaction steps		ΔH_r* $[\frac{kJ}{mole}]$
1	$CH_4 + 2O_2$	$\rightarrow CO_2 + 2H_2O$	-802.251
2	$2CH_4 + 1/2O_2$	$\rightarrow C_2H_6 + H_2O$	-175.710
3	$CH_4 + O_2$	$\rightarrow CO + H_2O + H_2$	-277.449
4	$CO + 1/2O_2$	$\rightarrow CO_2$	-282.984
5	$C_2H_6 + 1/2O_2$	$\rightarrow C_2H_4 + H_2O$	-105.668
6	$C_2H_4 + 2O_2$	$\rightarrow 2CO + 2H_2O$	-757.156
7	C_2H_6	$\rightarrow C_2H_4 + H_2$	136.150
8	$C_2H_4 + 2H_2O$	$\rightarrow 2CO + 4H_2$	-210.116
9	$CO + H_2O$	$\rightarrow CO_2 + H_2$	-41.116
10	$CO_2 + H_2$	$\rightarrow CO + H_2O$	41.166

*Reaction heats from Patcharavorachot et al. [12]

steps are considered to take place on the catalyst surface, except for the gas-phase dehydrogenation of ethane described by step 7. Furthermore, these ten steps can

be divided into three categories: The primary reactions converting methane (1-3), the secondary reactions further converting products of the primary reactions (4-6), and miscellaneous. The last category includes ethane dehydrogenation (7), ethylene reforming (8), and the water gas shift reaction in both directions (9, 10). Ideally, only reactions number 2 and 5 would occur, and the combustion reactions avoided as much as possible. The stoichiometries of the reactions in which oxygen participates suggest that the combustion reactions can be avoided by having relatively little oxygen present, and that is confirmed by the measured reaction orders: the reaction orders in oxygen are closer to one for the combustion reactions, while the selective reactions have oxygen reaction orders closer to one-half or even below that [10, 13]. The following conclusion has been central to all attempts to make a viable OCM reaction system: while decreasing the O_2 partial pressure slows down *all* of the reactions in which oxygen participates, the desired reactions are relatively slowed down much less.
A number of catalysts have been found to be active for OCM. Stansch has reported kinetics which were observed using a La_2O_3/CaO catalyst. Another catalyst which is very active is Mn-Na_2WO_4/SiO_2, and one of its major advantages is long-term stability. For this catalyst, kinetics have been reported by Daneshpayeh et al.[11, 13], and Shahri and alavi [14] (among others). These kinetics will also be considered because of their applicability to the more promising catalyst.
In theory, in situ product removal should also be an effective way of improving the process yield because of the consecutive nature of the reactions. In practice this proves infeasible because of the high temperature needed for the reaction, as all the possible separations (distillation, adsorption, membranes) are only effective at low temperatures. Because in situ product removal is infeasible, the consecutive nature of the reactions prevents reactor operation at high methane conversion: At conditions where methane conversion would be high, a significant quantity of the products would be lost. Therefore, the reactor effluent always contains a significant portion of unreacted methane.
Because of the inherent need to reduce the partial pressure of oxygen within the OCM reactor, simple co-feeding is not optimal. Also, distributed O_2 feeding also improves safety, which is not to be forgotten. In this thesis attention is paid to dense oxygen membrane reactors, and Solid Oxide Fuel Cells (SOFCs) which are conceptually the same regarding the oxygen distribution.

2.2 Membrane reactor and integration

As described in the previous section, a means of distributed feeding of oxygen is considered important. This can be achieved by integrating the OCM reactor with membranes. Because OCM is performed at very high temperatures, only inorganic membranes can be considered (as opposed to organic ones). Some of the concepts used here are also useful for the explanation of some aspects relevant to SOFCs. There are two distinct types of membranes: porous and dense. They are not only different in terms of transport mechanism, but also the resulting se-

lectivities and fluxes. Both have found their application in OCM research, and neither can yet be said to be better than the other. Porous membranes are briefly discussed for completeness, but not part of the research in this thesis for the sake of scope. Dense membranes are discussed in more detail, as they share more similarity with fuel cells.
Porous membranes are manufactured in such a way that the material features many pores: microscopic pathways or tunnels through which fluids may permeate. The sizes of the pores and the applied pressure drop determine the transport mode: for example, very small pore sizes can be used to prevent large molecules from permeating (nanofiltration). Also, surface interactions can facilitate the permeation of certain types of molecules more than others, and lastly, a higher pressure drop leads to a higher flux. In the case of OCM, the used molecules are much alike: they are all quite small, they are all non-polar except for water, and they are all in the gas phase. This means that porous membranes will not result in much selectivity: If air is used to dose oxygen, nitrogen will permeate the membrane just as well. Porous membranes have one great advantage: in general they exhibit greater fluxes compared to dense membranes.
Dense membranes allow the transport of a particular type of molecule without the use of pores. For the transport of oxygen, perovskites are the material class of choice for the fabrication of dense membranes [15]. Unlike porous membranes where gas molecules may permeate through channels, oxygen is dissociated into ions which can diffuse through the perovskite material. Not only is ion conduction allowing the permeation of oxygen ions by bulk diffusion, but the perovskite material is often also electrically conducting, allowing the electrons formed at the permeate side to travel back towards the retentate side and enable the whole process.

2.2.1 Flux descriptions

In order to do a modelling study, a mathematical expression for the oxygen flux is required. A well-established formulation is the Wagner equation [16]:

$$J_{O_2} = \frac{\sigma_0^i RT}{(n_e \mathbb{F})^2 n\delta}(P_{HO_2}^n - P_{LO_2}^n) \tag{2.1}$$

$\sigma_0^i, n_e, \mathbb{F}, n$, and δ respectively being the reference conductivity, number of electrons participating in the oxygen dissociation reaction, Faraday's constant, the oxygen pressure order, and the membrane thickness. $P_{HO_2}^n$ is used to denote the oxygen partial pressure at the side where it is highest, i.e. the retentate side. This equation is valid when the membrane is thick enough that bulk diffusion is slower than the rates of surface reactions of oxygen interconverting from molecular to ionic form.
Often this means that the membrane should be thicker than $500\mu m$ [17], but of course this depends on temperature and perovskite composition. A flux expression which takes account of the surface reaction rates as well as bulk diffusion

was published by Xu and Thomson [18]:

$$J_{O_2} = \frac{k_r D_V \left(P_{HO_2}^n - P_{LO_2}^n\right)}{k_f \delta P_{HO_2}^n P_{LO_2}^n + D_V (P_{HO_2}^n + P_{LO_2}^n)} \tag{2.2}$$

The variables k_r, D_V, and k_f are assigned Arrhenius-type dependencies. The oxygen pressure order n can be assigned a value experimentally, or given the theoretical value of 0.5. This theoretical value is generally applicable when the membrane has a thickness greater than $500 \mu m$. Consequently, that is the thickness which is used in this work, and n is set to $n = 0.5$. Whenever a membrane reactor is considered (so not a SOFC), a flux equation is used for a BCFZ perovskite, as this perovskite has been used OCM experiments [19]. The equation is shown in equation 2.2, and the necessary parameters are as follows (source: [20]).

$$D_V = exp\left(\frac{75.6 \cdot 10^3}{RT}\right) \qquad m^2\ s^{-1}$$

$$k_r = 1.1 \cdot 10^2 exp\left(\frac{83.28 \cdot 10^3}{RT}\right) \qquad mole\ m^{-2}\ s^{-1}$$

$$k_f = 2.9 \cdot 10^2 exp\left(\frac{268 \cdot 10^3}{RT}\right) \qquad m\ Pa^{-0.5}\ s^{-1}$$

The values are given in SI units, so the resulting flux is obtained in units $mole\ m^{-2}\ s^{-1}$.

2.3 Solid Oxide Fuel Cell

In a Solid Oxide Fuel Cell (SOFC), oxygen ions permeate a medium just as in a perovskite membrane. Therefore, it enables a conceptually similar reactor design. The most important difference is that electrical power can be obtained from operating a fuel cell. This leads to additional theoretical aspects which are discussed in this section. As discussed in section 1, two SOFC variants are investigated. They differ in the reaction which takes place in the anodic chamber, which will be OCM or methane reforming.

2.3.1 Physical outline of the fuel cell

A possible tubular SOFC design is shown in figure 2.1. Air flows past the outside of the cell, and chemicals are injected inside. The cell has a closed-cap structure at one end to reduce the number of seals. The feed tube is then necessary to facilitate efficient transport of fuel. In this thesis, the closed end and the feed tube are disregarded: This way the computationally intensive counter-current simulation is avoided, as the additional computational effort is not expected to be justified by a significant change in reactor performance.

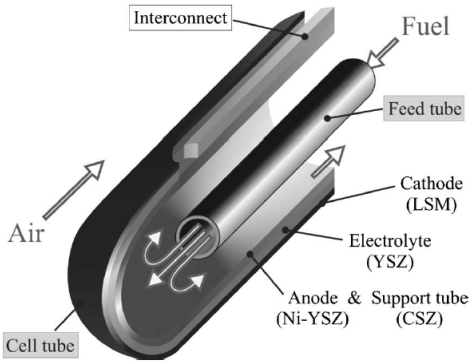

Figure 2.1: Schematic view of a tubular SOFC. Source: [21]

The cell tube consists of three layers which work together to transmit oxygen ions from the air to the fuel side. Respectively these are the cathode, the electrolyte and the anode. The anode is the electrode at the fuel side. In this design, the anode, electrolyte and cathode are deposited on a support tube, but the same design could also have been 'anode-supported' if the anode were made thick enough to be sufficiently strong. Along the top of the cell, the anode is not coated with the other two layers, but with an interconnect: this serves to establish a conductive path for the electrons so they can be transmitted back to the cathode. For oxygen molecules to be transported as ions, they have to undergo electrochemical transformation on the surface of the electrodes. This is similar to the surface reactions on perovskite membranes. In fact, the electrodes may be manufactured from perovskites [22]. Perovskites are both ionically and electronically conductive, meaning that the ions and electrons which are formed at the interfaces travel through the same medium.

Note that equal amounts must be exchanged: four electrons must be exchanged for each oxygen molecule. In an SOFC, an electrolyte is placed in between the two

electrodes, and its key feature is that it allows almost zero electronic conduction. Because of this, those four electrons per oxygen molecule must transported between the electrodes by another route. This is achieved by what is called the *external circuit*, which may just be some wire connecting the electrodes, or an actual application consuming electrical power. The electrolyte is often made of a fluorite, such as Yttria-stabilized Zirconia (YSZ)[21, 15]

2.3.2 Nernst Voltage

The circulation of electrons and the permeation of oxygen ions does not happen for free, electrical work must be done. This electrical work is generally described as the product of amount of charge transferred and the voltage:

$$W = -n_e \mathbb{F} E \tag{2.3}$$

The total transferred charge can also be written as $n_e\mathbb{F}$, where $\mathbb{F}$ is Faraday's constant (96485 Coulombe per mole electrons) and n_e is the number of electrons transferred per in the electrochemical reaction. The maximum electrical work could at most be equal to the maximum work done on the system, which is the Gibbs free energy change of the electrochemical reaction. Setting these equal and rearranging gives the following [23]:

$$E = -\frac{\Delta G}{n_e \mathbb{F}} \tag{2.4}$$

For a generic chemical reaction, the change in the Gibbs free energy can be written more explicitly:

$$aA + bB \rightarrow cC + dD \tag{2.5}$$

$$\Delta G = \Delta G_0 + RTln\left(\frac{C^c D^d}{A^a B^b}\right) \tag{2.6}$$

Using this, the nernst voltage is obtained by substitution [23]:

$$E = -\frac{\Delta G_0}{n_e \mathbb{F}} - \frac{RT}{n_e \mathbb{F}} ln\,(Q) \tag{2.7}$$

The cell voltage E in equation 2.7 is also known as the Nernst voltage V_{Nernst} [23]. In equation 2.7, R is the universal gas constant, T the temperature in Kelvin, n_e the number of electrons exchanged in the electrochemical reaction, and $\mathbb{F}$ is the Faraday constant ($\mathbb{F} = 96485\, C/mole\, e^-$). Q is the reaction quotient, i.e. the partial pressures of products divided by the partial pressures of reactants of the overall electrochemical reaction. Therefore it matters which electrochemical reaction is considered.

2.3.3 The electrochemical reaction

Which electrochemical reaction is performed within the fuel cell does not only depend on the reacting gases, but also on the electrocatalysts, i.e. the materials from which the electrodes are made. In the case of anodic reforming, the anode is a nickel cermet [21] which enables the electrochemical reaction of hydrogen with oxygen, as given in equation 2.8. For this reaction, $\Delta G_0 = -237.2\ kJ\ mole^{-1}$ [23].

In case of reforming:

$$\begin{aligned} \text{Cathode:} \quad & \frac{1}{2}O_2 + 2e^- \rightarrow O^{2-} \\ \text{Anode:} \quad & H_2 + O^{2-} \rightarrow H_2O + 2e^- \\ \text{Overall:} \quad & H_2 + \frac{1}{2}O_2 \rightarrow H_2O \end{aligned} \tag{2.8}$$

In the case of OCM, there will not necessarily be any hydrogen present. In order to facilitate a different anodic half cell reaction, the anode should be manufactured from a different material. In this thesis, it is assumed that the cathode material can also be used at the anode: LSM ($La_{1-x}Sr_xMnO_3$). In reality, few studies of OCM in SOFC have been performed. They have either been unclear about their choice of anodic material [24], or not mentioned it at all [25]. In any case, this is a materials science question which is of less importance to the modelling effort. In this work, the only consequence of this choice is in the electronic conductivity of the material. Assuming LSM is stable during use as the anode, it allows for the following electrochemistry [26]:

In case of OCM:

$$\begin{aligned} \text{Cathode:} \quad & \frac{1}{2}O_2 + 2e^- \rightarrow O^{2-} \\ \text{Anode:} \quad & O^{2-} \rightarrow \frac{1}{2}O_2 + 2e^- \\ \text{Overall:} \quad & O_2 \rightarrow O_2 \end{aligned} \tag{2.9}$$

This means that gaseous oxygen is formed on the anode surface, from where it diffuses towards the catalyst and participates in the OCM reactions normally. Since reaction 2.9 is not really a chemical reaction, the Nernst voltage (equation 2.7) is affected: the same equation is used, but with a standard Gibbs energy change of $\Delta G_0 = 0$ [26].

2.3.4 Kirchhoff's Law

The current density which is obtained during operation is determined by voltage losses. These losses include Ohmic losses, activation losses, and polarization

losses [27]. Furthermore, a portion of the voltage can be dedicated to power generation: this is the 'load voltage', and this is what is measured across the cell's terminals. The obtained power is defined as the product of the load voltage and the current I delivered by the cell, as in equation 2.10.

$$P = V_{load} \cdot I \tag{2.10}$$

Intuitively, the 'consumption' of voltage must equal the 'generation' of voltage: this is formalized in Kirchhoff's voltage law [28, 21], shown in equation 2.11.

$$V_{Nernst} + V_{load} + V_{Ohm}(J) + V_{act}(J) = 0 \tag{2.11}$$

Where the first term in the Nernst voltage as discussed in section 2.3.2, the second term is the load voltage, and the remaining terms are the voltage losses. It should be noted that that no term is included for the polarization loss, which is explained in section 2.3.7. At open circuit conditions (no current), the losses in equation 2.11 are zero, and the measured voltage should be equal to the Nernst voltage. However, the Nernst voltage is an idealization. Additionally, the measured voltage could be lower due to non-zero electronic conduction in the electrolyte, and small cracks in the electrolyte allowing the fuel to mix with the oxidant. Such losses can be considered by including an additional constant loss [27], but are neglected in this thesis. In equation 2.11, the Nernst voltage can be considered as a positive amount, and the remainder as negative. The losses depend on the current density J $\left(A\ m^{-2}\right)$: starting from given nernst- and load voltages, a current density must be found for which Kirchhoff's law is satisfied, and this is why the losses determine the current. Since equation 2.11 is nonlinear, the Newton-Raphson root finding method is used to solve it. Each of the voltage losses is discussed separately below. The load voltage is assumed constant [21]. How the constant load voltage is achieved is beyond the scope of this work.

2.3.5 Ohmic losses

The cell components with significant resistivities behave as linear resistors. The Ohmic loss occurring in a linear resistor is described by equation 2.12. However, it is useful to work in terms of the current density J (A m^{-2}), and then the Ohmic loss takes the form of equation 2.13.

$$V = IR \tag{2.12}$$

$$V = J\rho l \tag{2.13}$$

In equation 2.13, ρ is the electronic resistivity (a material property, units Ω m), and l is the length of the path over which the loss is calculated. This makes it easier to take account of various geometries. Ohmic losses can occur in multiple parts of the fuel cell. A schematic view of the electron path is given in figure 2.2, where the flow of electrons is indicated by black arrows. Starting arbitrarily from the interconnect, the electron path can be traced through the external circuit, into the

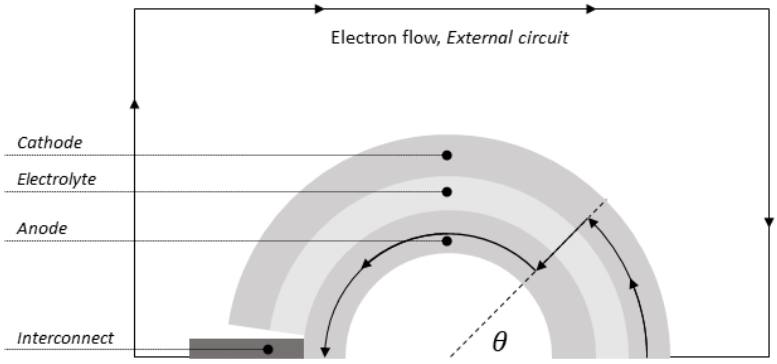

Figure 2.2: Electron path in a tubular SOFC (cross-section). Note that electrons only pass through the electrolyte in the form of oxygen anions

Table 2.1: Resistivity values. Source: [29]

Part	**Material**	**Resistivity** (Ω m)	**Resistivity type**
Cathode	LSM	$8.11 \cdot 10^{-5}\exp(600/T)$	Electronic
Electrolyte	YSZ	$2.94 \cdot 10^{-5}\exp(10350/T)$	Ionic
Anode	Ni-YSZ	$2.98 \cdot 10^{-5}\exp(-1392/T)$	Electronic

cathode, and finally through the electrolyte. It is important to note that the charge is not transferred across the electrolyte in the form of electrons, but in the form of oxygen anions. The anode releases the anions in the form of oxygen molecules and electrons complete the path back to the interconnect. The electron path is of concern because not only the electrolyte can have a significant (ionic) resisitivity, but also the electrodes [29]. The Ohmic loss depends on the path length l (see equation 2.13), which is a function of the angle θ when the losses in the electrodes are considered. In order to reconcile this with a model which assumes axi-symmetry (no θ-dependencies), the θ-averaged current density is taken. The used resistivity values are given in table 2.1.

The electrons are not transported across the electrolyte because the electronic resisitivity is much higher there. Electrons circulate through the external circuit because they seek the path of least resistance. The transport of ions through the electrolyte is also subject to voltage losses in the form of Ohm's law, but the ionic resisitivity is used and not the electronic resisitivity. The Ohmic loss is the sum of the Ohmic losses in the separate parts, as they occur in series along the electron path.

In the OCM case, the anode is assumed to be made of the same material as the cathode as discussed in section 2.3.3. Still, the θ-dependency of the current density

must be considered, because the path length l remains a function of the considered angle.
In reality, the Ohmic losses are dissipated as heat. The used solution method however does not allows for the solution of a heat balance in the solid, because there is no convection there. The model would have to be extended with the shooting method, or the entire model could be formulated as a root-finding problem. Instead, Ohmic heating is neglected.

2.3.6 Activation loss

The activation loss V_{act} is a loss occurring due to irreversibilities of the electrochemical reactions. It is implicitly expressed by the Butler-Volmer equation:

$$J = J_0 * \left(exp\left(\alpha \frac{n_e \mathbb{F}}{RT} V_{act} \right) - exp\left(-(1-\alpha) \frac{n_e \mathbb{F}}{RT} V_{act} \right) \right) \tag{2.14}$$

In this equation, J_0 is the exchange current density, and α the apparent charge transfer coefficient [30]. The implicit nature of equation 2.14 can make it cumbersome to compute the activation loss. However, it can be simplified by using $\alpha = 0.5$; this is often considered a safe assumption [31], and this value has experimentally been confirmed for an SOFC in which the reaction expressed in equation 2.8 was being carried out[32]. The simplification looks as follows:

$$J = 2 * J_0 \sinh\left(\frac{n_e \mathbb{F}}{RT} V_{act} \right) \tag{2.15}$$

This is computationally much simpler, as the inverse of the hyperbolic sine can be taken and the activation loss is found directly. J_0 has been expressed as a function of gas composition and an Arrhenius-type law [32]:

$$J_{0,c} = \gamma_c \left(\frac{p_{O_2}}{p_{ref}} \right)^{0.25} exp\left(-\frac{E_{act,c}}{RT} \right) \tag{2.16}$$

$$J_{0,a} = \gamma_a \left(\frac{p_{H_2}}{p_{ref}} \right) \left(\frac{p_{H_2O}}{p_{ref}} \right) exp\left(-\frac{E_{act,a}}{RT} \right) \tag{2.17}$$

As can be seen above, both the cathode and anode each have their own exchange current density J_0 associated with them. The smallest of them both is used to calculate the activation loss. Also, note that this formulation of the exchange current densities only makes sense when hydrogen is participating in the electrochemical reaction. When it isn't, such as in the OCM SOFC case, only the cathodic exchange current density from equation 2.16 is used. The parameters used in equations 2.16 and 2.17 are given in table 2.2.

Table 2.2: Exchange current density parameters. Source: [32]

Anodic reference exchange current density	γ_a	$5.5 \cdot 10^8$	A $m^{-2}s^{-1}$
Cathodic reference exchange current density	γ_c	$7 \cdot 10^8$	A $m^{-2}s^{-1}$
Anodic activation energy	$E_{Act,a}$	100	kJ $mole^{-1}$
Cathodic activation energy	$E_{Act,c}$	120	kJ $mole^{-1}$

2.3.7 Polarization loss

The polarization loss has to do with the fact that the concentration profiles might get polarized near the surface of the electrodes. In this case, the Nernst voltage is lower than if concentration polarization was absent. Since only bulk concentrations are measured experimentally, this causes a discrepancy between the measured voltage and the voltage which corresponds to a voltage which can be calculated from the measured concentrations using the Nernst voltage and accounting for losses. The difference between these measured and calculated voltages is called the polarization loss, and it can have an important effect on fuel cell performance. In a 2D modelling approach such as the one used in this work, the radial concentration profiles are resolved, and its account on the Nernst voltage accounted for. Therefore the polarization loss is inherently accounted for in a 2D model, no matter the degree of concentration polarization.

2.4 Methane reforming

In order to be able to use the outlet of an OCM reactor for power generation, the unconverted methane needs to be reformed. The hydrogen which is produced in this way is used in the fuel cells. One of the advantages of SOFC technology is that they operate at high enough temperatures that the reforming reaction can take place within the fuel cell itself. Since the OCM reactor outlet also contains significant amounts of CO_2, it is advantageous to use specialized catalyst (e.g. Ni-CeO_2/$MgAl_2O_4$) which not only allow for steam reforming of methane (SRM), but also dry reforming (DRM). When both are taking place, it can be referred to as mixed reforming. Of course, the water gas shift reaction (WGS) also takes place. The following reactions are considered [33]. These reactions are implemented using parameters and rate equations reported by H.J. Jun et al. (source [33]). The DRM reaction is central, because the of the assumptions concerning the separation of the C_2 products from the OCM reactor outlet before the remaining stream is introduced to the internal reforming SOFC: in order to separate the

Reaction			$^*\Delta H_r$	(kJ $mole^{-1}$)
SRM1	$CH_4 + H_2O$	$\rightleftharpoons CO + 3H_2$	206	*[34]
SRM2	$CH_4 + 2H_2O$	$\rightleftharpoons CO_2 + 4H_2$	165	*[34]
WGS	$CO + H_2O$	$\rightleftharpoons CO_2 + H_2$	-41	*[34]
DRM	$CH_4 + CO_2$	$\rightleftharpoons 2CO + 2H_2$	248	*[35]

OCM products, cryogenic distillation is the most widely-used technology. Before that can be done, water and CO_2 must be removed. In this thesis it is assumed that the CO_2 is reintroduced to the inlet of the reforming section. In this way, a dry stream enters the SOFC, but as soon as the DRM reaction takes place, hydrogen is produced which can be electrochemically converted to water. That water in turn reacts further with methane.

3 Model Description

In this section, the derivation of the mathematical model is discussed, as well as physical correlations. The numerical implementation and solution method are also explained.

3.1 Model structure

It is of interest to develop a model in cylindrical coordinates as this allows both the description of tubular membrane reactors as well as fuel cells with a tubular geometry. The model equations are formulated as Ordinary Differential Equations (ODEs) with respect to the axial coördinate z, which will be solved by an algorithm marching from the initial conditions at $z = 0$. This general approach has been successfully been applied before [9].

3.1.1 Derivation of governing equations

First, a ring-shaped control volume is defined as follows:

$$\Delta V_R = \Delta A \Delta z = \pi(r^2 - (r - \Delta r)^2)\Delta z \tag{3.1}$$

$$\Delta V = \varepsilon_g \Delta V_R \tag{3.2}$$

The model consists of the gas-phase balances, for which the relevant control volume is obtained by accounting for the gas fraction. Barring exceptions, reactions are expected to take place over the solid surface, and the source term appears in the balance over the solid phase. The gas- and solid phase balances are coupled by mass- and heat transfer terms. Steady state is assumed, so the source term in the mass balance is equal to the mass transfer term. As the mass transfer term also appears in the gas phase, the source term can be substituted into the gas phase (accounting for the correct units).
In equation 3.3 the gas phase mole balance is given describing axial convection, radial diffusion, and reaction. The axial diffusion is neglected as transport in that direction is assumed to be dominated by convection (which is to be made true by choosing an appropriate flow rate).

$$\frac{\partial N}{\partial t} = F_0 - F + \frac{1}{r} D_{eff,r} \frac{\partial}{\partial r}\left(r \frac{\partial c}{\partial r}\right) \Delta V + R \Delta V \tag{3.3}$$

Here mass diffusion is described by Fick's law, using an effective radial dispesrion coefficient $D_{eff,r}$ as described later on in section 3.2.1. None of the phenomena which Fickian diffusion has trouble describing, such as reverse diffusion due to intermolecular drag, are expected to occur in the reactor model. Heat conduction is described analogously using Fourier's law. Assuming steady state and dividing by the control volume gives the following:

$$\frac{\Delta F}{\Delta V} = \frac{1}{r} D \frac{\partial}{\partial r}(r \frac{\partial c}{\partial r}) + R \tag{3.4}$$

The ODEs which will be solved are then obtained by manipulation of the left-hand side and letting the control volume go to zero:

$$F = F_v \cdot C = \varepsilon_g \Delta A \cdot u \cdot C = \varepsilon_g \Delta A \cdot F'' \tag{3.5}$$

$$\frac{dF}{dV} = \frac{dF''}{dz} \tag{3.6}$$

Finally, the ODEs for the concentration look as follows:

$$\frac{\partial F''}{\partial z} = \frac{1}{r} D \frac{\partial}{\partial r}(r \frac{\partial c}{\partial r}) + R \tag{3.7}$$

In the case of heat transport, the derivation starts from a heat balance similar to the mole balance in equation 3.3, but with units J s^{-1} instead of mole s^{-1}. the integration variable becomes the axial flux of energy $H''(Jm^{-2}s^{-1})$, and the resulting ODE looks as follows:

$$\frac{\partial H''}{\partial z} = \frac{1}{r} \lambda_{eff,r} \frac{\partial}{\partial r} \left(r \frac{\partial T}{\partial r} \right) + R(-\Delta H_R) \tag{3.8}$$

Here, $\lambda_{eff,r}$ is the effective thermal conductivity, accounting not only for the conductivity of the gases, but also that of the catalytic bed. This is described later in section 3.2.2.
Mathematically speaking, equations 3.7 and 3.8 are not ODEs at all, because they depend on the r coördinate in addition to the z coördinate. The numerical implementation is done in such a way that the radial dependencies can be satisfactorily accounted for at each z position without using information from any other z positions. This can be called the method of lines.

3.1.2 Numerical solution method

The radial direction of the numerical domain (the reactor) is discretized by choosing an integer amount of nodes at which the mole- and heat balances will be solved. The system of nodes can also be referred to as the grid, and the space in between the nodes is referred to as the cells.
At least two nodes must be used in the radial direction: one each at the beginning and end. If a fixed bed reactor is modelled (i.e., no membrane), this translates to

one node on the central axis of the reactor, and one on the inside of the wall. Any number of nodes can be chosen in between these two to increase computational accuracy.
In the case of a shell- and tube setup, the radial direction consists of two corresponding parts, which each require two nodes. In addition to the two that were already needed before, the inner and outer surface of the membrane each get a node.
Having access to the variables on the membrane surface is convenient for the computation of the flux. Similarly, accounting for heat conduction through the membrane and the reactor wall is facilitated by having the nodes on the respective surfaces.
Having chosen an appropriate number of nodes, the initial conditions are given at $z = 0$, where the integration will start and march in the axial direction.
The differential equations are then integrated using one of MatLab's built-in solvers, preferrably ode15s. The solver will start integrating the differential equations in the axial direction. The given relative tolerance as well as the absolute tolerance is used to determine acceptable step sizes. Because of that, more stringent (smaller) tolerances will cause smaller step sizes, and longer computation time.

3.1.3 Discretization of radial transport

As discussed, there is transport of heat and mass in the radial direction. These diffusive terms are discretized using second-order finite differences.
The factor $1/r$ in the diffusion term leads to singularity in the center of the system where $r = 0$. l'hopital's rule is used to avoid that, and the result is as follows [36]:

$$\frac{1}{r}D\frac{\partial}{\partial r}\left(r\frac{\partial c}{\partial r}\right) = D\frac{\partial^2 c}{\partial r^2} + D\frac{1}{r}\frac{\partial c}{\partial r} \tag{3.9}$$

$$= 2D\frac{\partial^2 c}{\partial r^2} \tag{3.10}$$

Which is only valid at $r = 0$. Over the remaining range of r values, a second discretization is needed; both are given below [36]:

$$\frac{1}{r}D\frac{\partial}{\partial r}\left(r\frac{\partial c}{\partial r}\right)\Big|_{r>0} = \frac{1}{r^i}D\frac{1}{\Delta r^2}(r^{i+1/2}(c^{i+1} - c^i) - r^{i-1/2}(c^i - c^{i-1})) \tag{3.11}$$

$$\tag{3.12}$$

$$\frac{1}{r}D\frac{\partial}{\partial r}\left(r\frac{\partial c}{\partial r}\right)\Big|_{r=0} = 2D\frac{\partial^2 c}{\partial r^2} \tag{3.13}$$

$$= 2D\frac{1}{\Delta r^2}(c^{i+1} - 2c^i + c^{i-1}) \tag{3.14}$$

Superscript i refers to the i^{th} node in the radial direction.

3.1.4 Boundary conditions

The boundaries of the domain are as follows:

- The inlet
- The outlet
- The central axis
- The membrane surfaces
- The outer wall

For all components (mass and energy), the inlet and outlet are simple: In fact, they are not really set in the same way due to the nature of the solution method. The inlet is set as a Dirichlet condition (constant values), and the outlet is freely allowed to be whichever value is arrived at by the solver. The boundary at the central axis is set as Neumann (no flux). This is also known as a symmetry condition, and can not be chosen differently without violating the axi-symmetric assumption of the equations laid out in section 3.1.1.

$$D_{eff,r}\frac{\partial C}{\partial r}\Big|_{r=0} = 0 \tag{3.15}$$

$$\lambda_{eff,r}\frac{\partial T}{\partial r}\Big|_{r=0} = 0 \tag{3.16}$$

For the tube and shell sides of the membrane surface, the flux of oxygen must be set:

$$\text{Tube side: } D_{eff,r}\frac{\partial C}{\partial r}\Big|_{r=R} = J \tag{3.17}$$

$$\text{Shell side: } D_{eff,r}\frac{\partial C}{\partial r}\Big|_{r=R+\delta} = -J\frac{R}{R+\delta} \tag{3.18}$$

Where R is the inner radius of the tube, and δ the thickness of the membrane. The factor $\frac{R}{R+\delta}$ appears in order to preserve mass conservation: this would be violated if the same flux J (mole $\mathrm{m}^{-2}\mathrm{s}^{-1}$) were applied to the larger surface area at position $r = R+\delta$. An important assumption that goes into this is that the smaller membrane area at $r = R$ limits the mass transfer. Similar boundary conditions on the membrane surface are used for heat transfer:

$$\text{Tube side: } \lambda_{eff,r}\frac{\partial T}{\partial r}\Big|_{r=R} = \Phi \tag{3.19}$$

$$\text{Shell side: } \lambda_{eff,r}\frac{\partial T}{\partial r}\Big|_{r=R+\delta} = -\Phi\frac{R}{R+\delta} \tag{3.20}$$

Here, Φ is determined by assuming a linear temperature profile within the membrane:

$$\Phi = \lambda_{eff,r}\frac{T|_{r=R} - T|_{r=R+\delta}}{\delta} \tag{3.21}$$

The same principle is used at the outer wall. Of course, there the mass flux J is zero.
The temperature which is considered to be constantly applied at the outer wall is equal to the inlet temperature. This has been chosen in modelling experimental cases, where a single tube is placed inside a temperature-regulating furnace. However, this boundary condition is expected to be much less applicable to full scale reactors in industrial application: Many small tubes (be they membrane reactors or fuel cells) are expected to be operated with only minimal distance in between them. Therefore, the boundary condition for the temperature would not be constant, but subject to more complex behaviour.

3.2 Correlations

A few correlations are included in the model, which is discussed in more detail below. Also the calculation of some other run-time variables is addressed here.

3.2.1 Effective diffusivity

Since only gas phase balances are solved, correlations are needed for the diffusivity and thermal conductivity. In the case of diffusion, the effective diffusivity (or dispersion coefficient) is not equal to the molecular diffusivity because the fluid is not stagnant, and it encounters a complicated flow path through the catalyst particle interstitial areas. The following correlation is used [37][38]:

$$D_{eff,r} = \left(1 - \sqrt{1-\varepsilon_s}\right) D_m + \frac{u \cdot d_p}{Pe} \tag{3.22}$$

$$Pe = 8.65 \left(1 + 19.4 \left(\frac{d_p}{d_t}\right)^2\right) \tag{3.23}$$

Where ε_s is the solids volume fraction, u the superficial velocity, and Pe the Peclet number. Strictly speaking, the molecular diffusivity D_m varies between chemical species as well as with temperature. It is taken as $2 \cdot 10^{-5}$ as an approximation, and the resulting $D_{eff,r}$ is used for all species. u is the superficial velocity, d_p the particle radius, d_t the tube diameter, and ε the solids volume fraction, equal to 64%.

3.2.2 Effective thermal conductivity

A correlation for the thermal conductivity is needed for the same reason of non-stagnant fluid, but also because the contribution of heat transport through the solids must be accounted for. The following correlation is used [39]:

$$\lambda_{eff,r} = \lambda_{conv} + \lambda_{cond,rad} \tag{3.24}$$

$$\lambda_{conv} = \frac{\rho c_{p,gas} u X_f}{8\left[2 - \left(1 - \frac{2d_k}{d_t}\right)^2\right]} \tag{3.25}$$

$$\lambda_{cond,rad} = \lambda_f \left(1 - \sqrt{1-\epsilon}\right) \epsilon \left[(\epsilon - 1 + k_G^{-1})^{-1} + \lambda_{rad}\right] + \sqrt{1-\epsilon}[\phi k_p + (1-\phi)k_c] \tag{3.26}$$

The calculation of remaining constants such as k_c is done as follows:

$$k_c = \frac{2}{N}\left\{ \frac{B(k_p + k_{rad} - 1)}{N^{2k_G k_p}} \ln \frac{k_p + k_{rad}}{B[k_G + (1-k_G)(k_p + k_{rad})]} \right. \tag{3.27}$$

$$\left. + \frac{B+1}{2B}\left[\frac{k_{rad}}{k_G} - B\left(1 + \frac{1-k_G}{k_G}k_{rad}\right)\right] - \frac{B-1}{Nk_G} \right\} \tag{3.28}$$

$$N = \frac{1}{k_G}\left(1 + \frac{k_{rad} - Bk_G}{k_p}\right) - B\left(\frac{1}{k_G} - 1\right)\left(1 + \frac{k_{rad}}{k_p}\right) \tag{3.29}$$

$$l_\gamma = 2\frac{2-\gamma}{\gamma}\sqrt{\frac{2\pi RT}{M}}\frac{\lambda_f}{p\left(\frac{2c_{p,g}}{M} - \frac{R}{M}\right)} \tag{3.30}$$

$$B = C_f \frac{1 - \epsilon^{10/9}}{\epsilon} f(\xi) \tag{3.31}$$

$$\lambda_{rad} = \frac{4\sigma}{\frac{2}{\epsilon^f} - 1} T^3 d_k \tag{3.32}$$

$$k_p = \frac{\lambda_s}{\lambda_f} \tag{3.33}$$

$$k_G = \left[1 + \frac{l_\gamma}{d_k}\right]^{-1} \tag{3.34}$$

$$X_f = 1.15 \tag{3.35}$$

$$C = 1.25 \tag{3.36}$$

$$\sigma = 5.6704 \cdot 10^{-8} \tag{3.37}$$

$$f(\xi) = 1 \tag{3.38}$$

Using these correlations with a gas phase thermal conductivity of 0.17 (methane gas), and a solid phase thermal conductivity of 1.4 (silica catalyst support [40]), an effective thermal diffusivity is found with the value of $\lambda_{eff,r} \approx 0.91$

3.2.3 Pressure drop

Due to the presence of catalytic packing in a reactor section, a pressure drop is to be expected. The pressure drop is of course described by the Ergun equation [41] as shown in equation 3.39.

$$\frac{\Delta p}{L_R} = 150\frac{\mu}{d_p^2}\frac{(1-\varepsilon_g)^2}{\varepsilon_g^3}u + 1.75\frac{\rho_g}{d_p}\frac{(1-\varepsilon_g)}{\varepsilon_g^3}u^2 \tag{3.39}$$

Note that here the particle sphericity has been assumed equal to one.

3.2.4 Run-time properties

As discussed in section 3.1, the input to the ODE function consists of mole fluxes F'' (mole m^{-2} s^{-1}) and heat fluxes H'' (J m^{-2} s^{-1}). However, the various phenomena of reactions, diffusion, and thermal conduction are driven by different properties: partial pressures, temperature, and differences in concentration and temperature. It is shortly shown how those are calculated from the input.
The local pressure is calculated from the inlet pressure and the pressure drop as follows:

$$p(z) = p(z = 0) - \frac{\Delta p}{L_R} \cdot z \tag{3.40}$$

Where both $p(z = 0)$ and $\frac{\Delta p}{L_R}$ are calculated during model initialization, and the pressure profile is assumed linear. Specifically, an outlet pressure is chosen and the inlet pressure is calculated from that. This has the advantage that the in- and outlet pressures are known during initialization, which is not the case when treating Ergun's equation as an additional ODE to be solved.
The temperature is calculated from the volumetric energy density H (defined in section 3.1) taking account of the effect of the composition of the mixture:

$$T = \frac{H''}{\Sigma_{i=1}^{N} \left(M_{w,i} F_i'' C_{p,i}\right)} \tag{3.41}$$

With the pressure temperature known, the total concentration can be calculated using the ideal gas law. From the total concentration and the mole fractions the concentrations are re-calculated. The concentrations are already given as input, but re-calculating them in this way assures that they follow the equation of state. The mole fractions are simply calculated from the mole flows F_i as follows:

$$x_i = \frac{F_i''}{\sum_{i=1}^{N} \left(F_i''\right)} \tag{3.42}$$

With the mole fractions, the partial pressures can also be calculated from the total pressure.

4 Model Evaluation

It must be evaluated to what extent the model can be trusted. This consists of verification (checking the model mathematically), and validation (comparing the model's predictions to experimental results). Before the validation section, the selection of the kinetic model for OCM is discussed.

4.1 Verification

A number of verification studies have been performed in order to confirm that the various aspects of the model are free of mathematical errors. First the very simplest case (convection only) is considered, and the complexity is increased from there. A relative error can be defined between the numerical solution $S_{numerical}$ and the exact solution S_{exact} as in equation 4.1.

$$\varepsilon_{rel} = (S_{exact} - S_{numerical})/S_{exact} \tag{4.1}$$

4.1.1 Convection-reaction

First a verification study is presented for the case of flow under constant superficial velocity with the chemical species undergoing a first order reaction isothermally. This corresponds to the analytical solution shown in equation 4.2.

$$C(z) = C_0 \cdot exp\left(-\frac{k}{u}z\right) \tag{4.2}$$

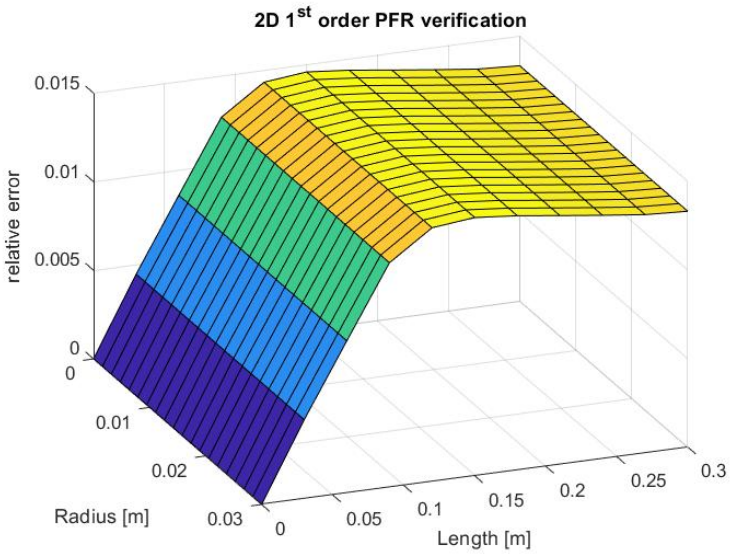

Figure 4.1: Relative error of convection-reaction case

In equation 4.2, C_0 is the inlet concentration, k the first order rate constant, u the superficial velocity, and z the axial coordinate. Due to the lack of thermal effects, there are no radial dependencies. This can be seen in figure 4.1. This case has been implemented in 2D rather than 1D because in that way, it not only serves as a verification of the mathematical model, but also as a check of the implementation of the 2D model. Most importantly the relative error is around 1%, which is considered acceptable.

4.1.2 Membrane convection-diffusion

The second case concerns permeation through a membrane. Mass conservation is tested. No analytical solution of the radial profiles is presented. In that sense it is not a verification study, but it is useful nonetheless. On the tube side of the membrane, air flows at 150 mL/min. On the shell side, pure nitrogen flows at 30 mL/min. Oxygen is permeates to the shell side as described by an arbitrary flux which scales with the difference in partial pressures between the compartments. At these conditions, the relative mass error was about $\varepsilon = 5 \cdot 10^{-4}$, defined as the mass going in minus the mass going out. It is concluded that the model very adequately describes the convection-diffusion phenomenon in the presence of a membrane.

4.2 Comparison of kinetic models

There are a few kinetic models. Those of the of the following authors are investigated:

- Stansch et al. [10]
- Daneshpayeh et al. [13]
- Shahri and Alavi [14]

Stansch et al. researched the La_2O_3/CaO catalyst, while the other two have investigated Mn-Na_2WO_4/SiO_2. Some times the 'Stansch kinetic' is also used for modelling activities concerning other catalysts, because desirable behaviours are observed such as correct (thermal) trend prediction. A set of experimental results using the Mn-Na_2WO_4/SiO_2 catalyst will be modelled. In the experiment, the reactor performance was investigated as a function of temperature in co-feed. All parameters (diameter, flowrate, temperature, etc.) are set the same. One uncertain parameter was the set temperature of the furnace in which the reactor tube was placed. This was assumed to be equal to the inlet temperature. Specifically, the goal is to determine which kinetic model best models the temperature dependence of OCM in a co-feeding reactor structure. Note that in figures 4.2, 4.3, and 4.4, the experimental data is indicated with dashed lines, while the simulation results are plotted with continuous lines.

4.2.1 Stansch et al.

Inserting the kinetic parameters of Stansch et al. resulted in a reactor performance which is shown in figure 4.2. It is immediately apparent that these results do

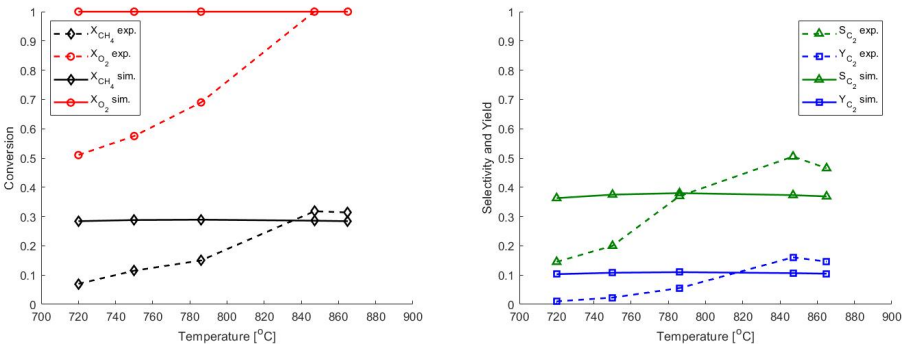

(a) Conversions **(b)** Selectivities/Yields

Figure 4.2: Comparison between experimental data (dashed, [42]) and simulation (continuous) with Stansch kinetic parameters

not seem to vary enough with temperature. First of all, it is worth noting that complete oxygen conversion is achieved in all cases. The underlying cause is that the entire overall reaction process was much faster in the simulation than it was in the experiment. This also results in a temperature rise over one hundred degrees within the first few centimeters of the reactor. It seems that at this regime of high reaction intensity (compared to the flow rate), the selectivity is much more strongly determined by the C/O ratio than it is by the temperature. In any case, this validation is not satisfactory, and does not indicate the model using Stansch kinetics has any power to predict the temperature dependence of OCM during co-feeding over the chosen catalyst.

4.2.2 Daneshpayeh et al.

It must be noted that the kinetics which were originally published by this author ([11]), do not give satisfactory results (out of the three primary reactions, the rate of complete methane combustion dominates in magnitude), and Daneshpayeh published a corrected set of kinetic parameters later the same year [13]. Parameters from that second publication are used in this thesis. It can be seen in figure 4.3 that the model now follows some trends much better: the methane conversion and oxygen conversion increase with temperature as the catalyst becomes more activated, and the yield goes through a maximum at the fourth data point. However, the methane conversion is overestimated, in turn leading to an overestimation of the yield. The latter is quite a significant overestimation, because the selectivity is also overestimated at all temperatures. This overestimation ex-

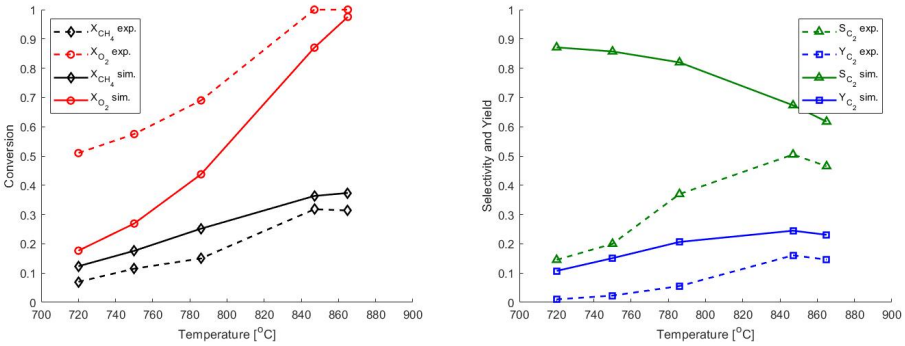

(a) Conversions **(b)** Selectivities/Yields

Figure 4.3: Comparison between experimental (dashed, [42]) data and simulation (continuous) with Daneshpayeh kinetic parameters

plains why less oxygen is converted than in the experiment. Also, it is a problem that the simulation shows no selectivity optimum as a function of temperature, as is visible from the experiment. This validation cannot be called successful, but further investigation is warranted.

4.2.3 Shahri and Alavi

Another kinetic model has been published by Shahri and Alavi, concerning the Mn-Na_2WO_4/SiO_2 catalyst. The simulated result is shown in figure 4.4. Here, the

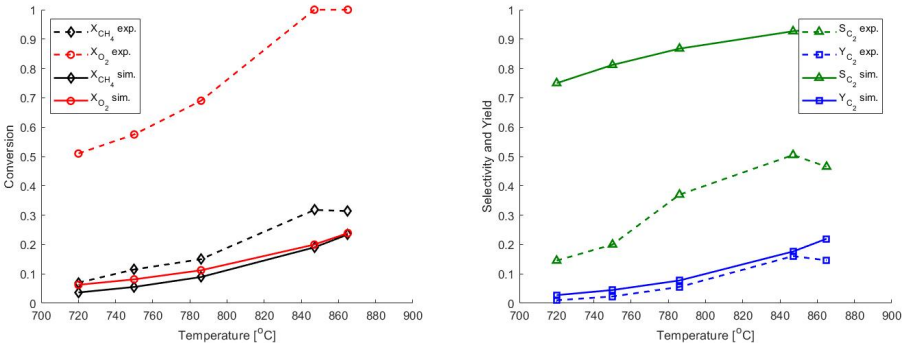

(a) Conversions **(b)** Selectivities/Yields

Figure 4.4: Comparison between experimental (dashed, [42]) data and simulation (continuous) with Shahri kinetic parameters

C_2 yield is the most accurate amongst the three compared kinetic sets. However, it is a complete coincidence: the vast overestimation of the selectivity is counteracted by the underestimation of the conversion. As to the trends predicted with

these kinetics: they all seem quite good, except for the lack of an optimum in the selectivity. Despite this, the quantitative disagreement with the experiment is too great, and this model will not be considered further.

4.3 Validation

In this section, simulations are more rigorously compared to experimental results. In section 4.2 some results were presented as a function of temperature. However, it is worthwhile looking more closely at the thermal behaviour. Therefore, a single experiment was selected for which the temperature profile was reported along with the reactor performance. This is presented below as the co-feed case. Furthermore, a distributed-feed case is investigated, as the more important simulated results in this thesis will also be considering distributed feeding.

4.3.1 Co-feed case

The selected experiment is one where a mixture of methane, oxygen and nitrogen are co-fed into a bed packed with Mn-Na_2WO_4/SiO_2 catalyst. The comparison is drawn both in terms of reactor performance (methane conversion and C_{2+} yield as well as selectivity), and in terms of the temperature profile. This temperature profile was obtained experimentally with a thermocouple in the central axis of the bed. In the model, the presence of the thermocouple is ignored and the center is considered to also be filled with catalyst.
First of all, a grid study was performed, which resulted in a minimum number of radial nodes of 15. In figure 4.5, the area between the vertical dashed lines indicates the position of the catalytic bed. Methane, oxygen and nitrogen were co-fed at a ratio of 3:1:2.5. A simulation of the same system was performed using both the Daneshpayeh and Stansch kinetic models. In table 4.1, the reactor performance in both the experiment and the simulations are given. Furthermore, the temperature profile that was obtained through simulation with Daneshpayeh kinetics is plotted along with the graph of the experimental temperature profile in figure 4.5. First, the Daneshpayeh results are compared to the experiment. Roughly the same conversion is obtained in the simulation, but an 18% higher selectivity is exhibited, causing a higher yield as well. This can be explained by looking at the temperature profile: in the experiment, the temperature starts rising before the reactants have reached the catalyst bed. This means that gas phase reactions are taking place. These are of course less selective than their heterogeneously catalyzed

Table 4.1: Comparison of reactor performance in co-feed. Source: [43]

	Experiment	Sim. (Daneshpayeh)	Sim. (Stansch)
CH_4 Conversion	36%	35%	25%
C_{2+} Selectivity	60%	78%	7%
C_{2+} Yield	19%	27%	2%

counterparts. In the Daneshpayeh kinetics all of the primary reactions are heterogeneous, and therefore nothing happens until the catalyst bed is reached. The selectivity is better in the simulation, and the desired reactions are less exothermic than the undesired ones. This explains the smaller temperature rise in the simulation. Lastly, the temperature decrease after the maximum proceeds more slowly in the simulation: this is because oxygen is only 70% converted in the simulation. The lower oxygen conversion is also a result of the overestimated selectivity, as the desired reactions consume relatively less oxygen. The ongoing release of heat makes the gas cool down more slowly than in the experiment, where oxygen is presumably completely converted before exiting the catalyst bed. Considering the above, the best remedy would be to include gas phase reactions in the simulation. However, no kinetic model has been published which considers both the heterogeneous and homogeneous reaction pathways. In conclusion: the main differences between the experiment and the simulation here are due to the unmodeled presence of gas-phase reactions, a discrepancy which causes a significant over-estimation of the selectivity. However, the thermal behaviour seems adequately modelled considering that limitation. This kinetic model allows for a reasonable reproduction of experimental results, and this could even be better for distributed-feed cases where gas-phase reactions are expected to play a less significant role. The simulation using the Stansch kinetic model was less successful.

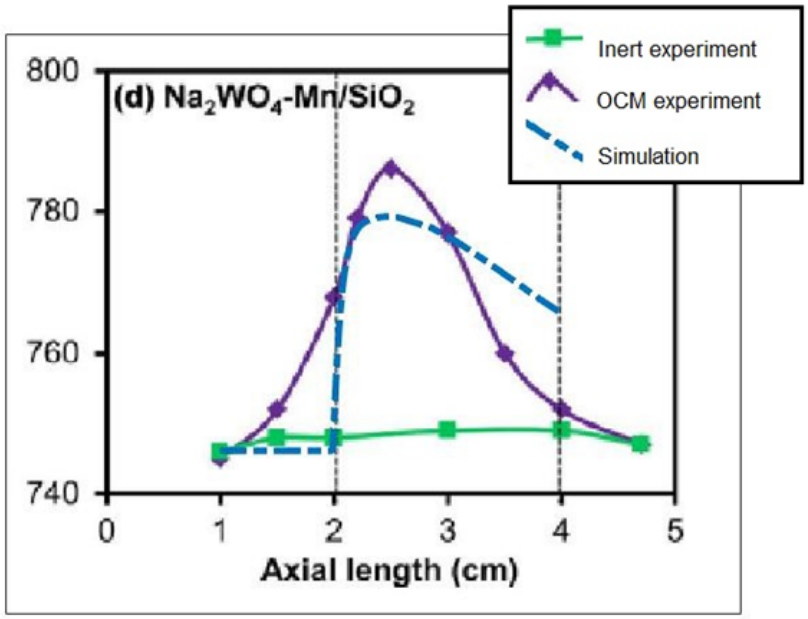

Figure 4.5: Comparison of experimental and simulated temperature profiles in the central axis. Kinetic model: Daneshpayeh. Data source: [43]

It must be noted that here the catalyst density was used which corresponds to the catalyst which was used in the experiment ($\rho_{cat} = 600$ kg/m^3), instead of the catalyst density from Stansch's publication, which is higher. The temperature rise in the Stansch co-feed simulation is more than a 1000 K, in clear disagreement with the experiment. The Stansch kinetic vastly overestimates the activity of the catalyst, which causes oxygen to be fully converted within the first few millimeters of the catalyst bed length. The selectivity is probably already underestimated by the Stansch kinetic model, but that is exacerbated by the rapid temperature rise caused by the overestimated activity. These disagreements are large enough that the lack of gas phase reactions seems to not matter. The undesired reactions consume more oxygen stoichiometrically speaking, which is why the methane conversion is lower despite full conversion of oxygen. The Stansch kinetic model is clearly not a good fit for the simulation of co-feeding reactor setups with the Mn-Na_2WO_4/SiO_2 catalyst.

4.3.2 Distributed-feed case

For the distributed-feed case, an experiment was selected where oxygen was dosed by exposing the tube side of a BCFZ ($BaCo_xFe_yZr_zO_{3-\delta}$) perovskite membrane to an air flow. The shell side was packed with the same OCM catalyst as was considered in the co-feed case (Mn-Na_2WO_4/SiO_2), and a methane flow was introduced there. A number of experiments were performed as a function of the oxygen concentration: that is to say, the air was diluted with additional nitrogen to control the oxygen fraction, and then passed along the retentate side of the membrane. In order to model this system, an expression is needed for the flux through the membrane. A Wagner equation such as first shown in equation 2.1 was fitted (eq. 4.3) to experimental data of oxygen permeation through a BCFZ membrane. The author discussed the applicability of the Wagner equation and determined the oxygen pressure order n to be $n = 0.25$, but did not provide all the needed parameters. The fitted expression is given in equation 4.3.

$$J_{O_2} = \sigma_0 \frac{R(T - T_0)}{(4\mathbb{F}^2)n\delta} \left(P^n_{HO_2} - P^n_{LO_2}\right) \tag{4.3}$$

The factor T was replaced by $(T - T_0)$ in equation 4.3. This is not physical, but it improves the quality of the fit by a factor 100. The result of the fit is shown in figure 4.6. The fit is not considered valid outside of the fitted temperature range, but the validation case in question is performed just within this range (800°C). The flux is around 0.1 cm^{3}cm^{-2}s^{-1} which is quite low but it seems applicable given the results of the simulations using this equation, shown in figures 4.7 and 4.8.
The results which are obtained when the system is modelled with Daneshpayeh kinetics is shown in figure 4.7. The data markers are made the same, i.e. methane conversion is marked with squares in both the experimental graph and the simulation results. What can be seen in figure 4.7 is that the simulation is not a very good match. Mostly, the methane conversion and selectivities show a very

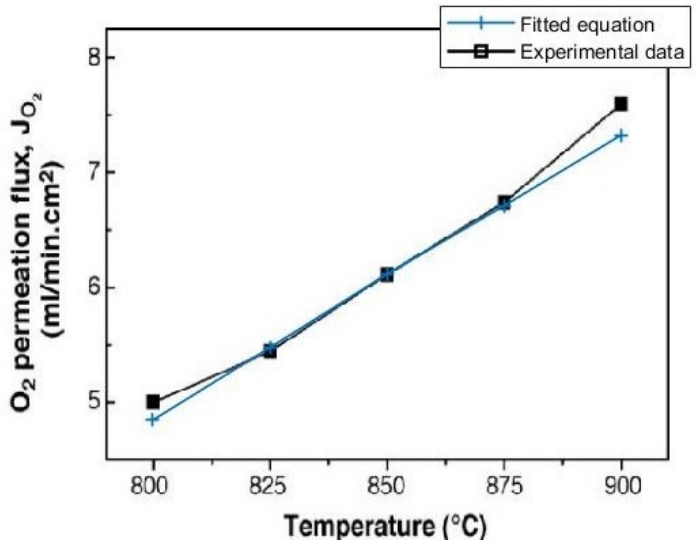

Figure 4.6: Wagner equation fit to experimental data. Source [44]

weak sensitivity towards the oxygen concentration. The most similar result is the carbon dioxide selectivity. Ethylene selectivity is very low while is should be relatively high, and ethane selectivity is high while it should be relatively low. On the other hand, the combined selectivities of ethylene and ethane are quite close. The methane conversion and C_2 yield are much too low as well.

The combined selectivity towards carbon oxides is pretty accurate, but the simu-

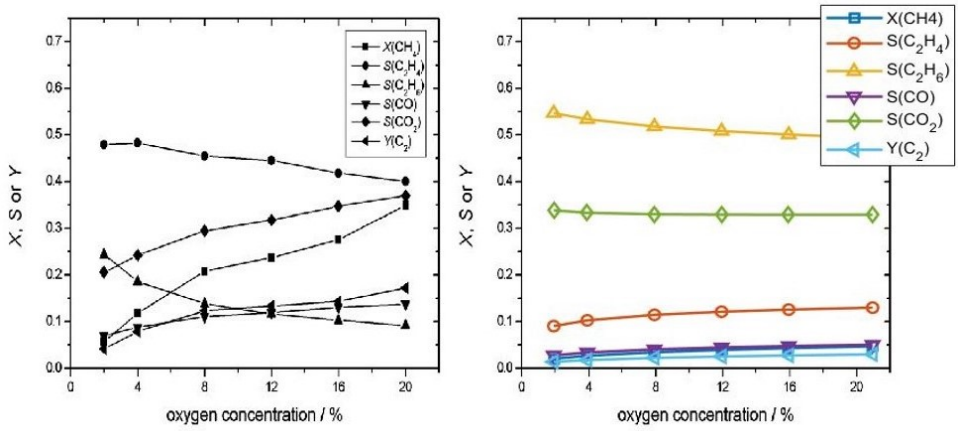

Figure 4.7: Distributed-feed case modelled with Daneshpayeh kinetics. Source: [19]

lation always favors CO_2 formation strongly while in the experiment much more CO was formed at lower oxygen concentration. The overall C/O ratios of the two cases are similar. The model does not reproduce the experimental results

with great accuracy, but it is passable. The same case was also investigated with

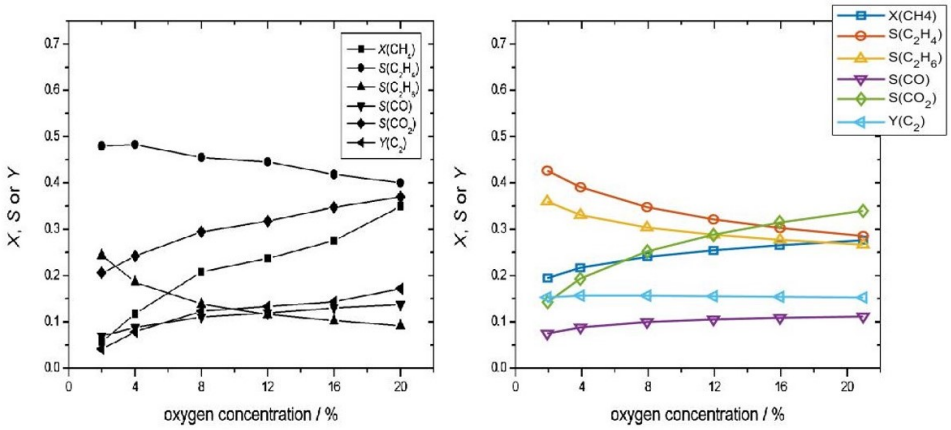

Figure 4.8: Distributed-feed case modelled with Stansch kinetics. Source: [19]

the Stansch kinetics. The result is shown in figure 4.8. Again, the data markers are the same. Here most of the trends are in agreement with the experiment, and the quantitative agreement is also much better. The worst disagreement is at low oxygen concentration, where the methane conversion and C_{2+} yield are overestimated. Also, ethane selectivity is overestimated over the entire range. Still, it seems that the Stansch kinetics perform quite well in predicting the behaviour of the investigated catalyst, despite having been measured for a different one.
The overestimation of the catalyst activity seems not to happen during distributed-feeding. This is not only shown by the quantitative agreement between experiment and simulation, but also because the temperature rise is much less extreme in this case (not depicted).

4.4 Comparison of Daneshpayeh and Stansch kinetic models

It is curious that the distributed-feed case validation with Daneshpayeh kinetics was not nearly as good as the co-feed case with Daneshpayeh kinetics. The selectivity C_2 products is supposed to be improved by distributed O_2 feeding, but the opposite was shown by the simulations: The selectivity was overestimated in co-feed while it was roughly similar to the experiment in the distributed-feed case. The distributed-feed case was not quite satisfactory. However, a comparison between the reactor performances between these simulations is not well justified, as the operating conditions are different.
Therefore, two cases have been simulated with the Daneshpayeh kinetics which are comparable. The co-feed case was taken as a basis, but the flow rate was decreased in order to obtain complete oxygen conversion. The distributed-feed case was constructed by taking the same reactor dimensions, but removing the oxygen and nitrogen from the feed, and instead changing the boundary conditions to

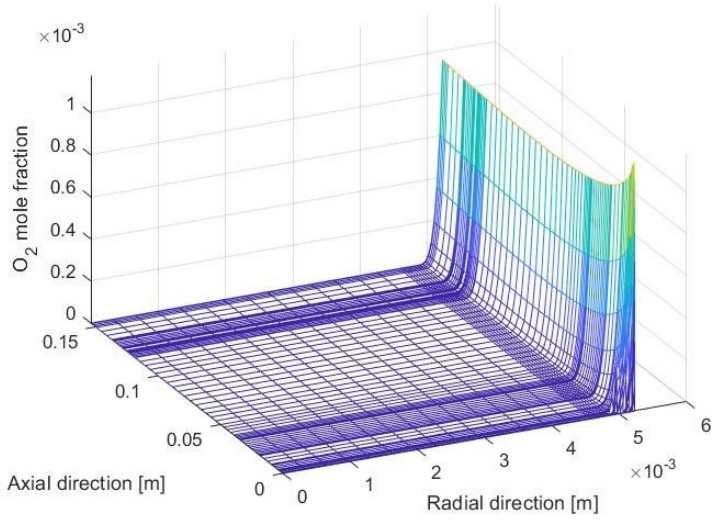

Figure 4.9: Mole fractions of oxygen in a distributed-feed case simulation. A smaller radial grid size was used near the membrane.

simulate the presence of a membrane. The used expression is of the form of equation 2.2 as reported by Xu & Thomson, with parameters for a BCFZ perovskite membrane [20]. The flow rate in the distributed-feed case was adjusted to obtain a conversion similar to the co-feed case, and both have an overall C/O ratio close to 3. The results are shown in table 4.2. Again, lower C_{2+} selectivity is obtained.

Table 4.2: Comparison of Daneshpayeh kinetics in co- and distributed-feeding

	Co-feed	Distributed-feed
CH_4 Conversion	42%	39%
C_{2+} Selectivity	70%	36%
C_{2+} Yield	29%	14%

While both cases have an overall C/O ratio around 3, the local C/O ratios differ greatly. In co-feed, a significant portion of the reaction occurs at local ratios similar to the overall ratio. However, in the distributed-feed case the local ratios of the order 100, and this is supposed to result in high selectivity. An example of the low mole fractions of oxygen can be seen in figure 4.9. At this point, a closer look at the kinetics is interesting. The improved selectivity at higher C/O ratios is expected because that corresponds to low oxygen pressures, and the desired reactions are supposed to have lower reaction orders in oxygen. This is considered common knowledge based on the widespread Stansch kinetic model, but is not true for the Daneshpayeh set of parameters. Out of the three primary reactions, reaction 2 is the desired one. In the Daneshpayeh kinetic, the reaction orders in oxygen are $n_1 = 0.5$, $n_2 = 0.75$, and $n_3 = 1.57$.

First, the instantaneous selectivity will be discussed, which can be formulated as shown in equation 4.4 [45]. This is the instantaneous selectivity of reaction 2, i.e. the formation of ethane.

$$S_2 = \frac{r_2}{\sum_{i=1}^{N} r_i} \tag{4.4}$$

This is defined in terms of reaction rates rather than in terms of product flow rates as usual, and is useful because the kinetics can be evaluated without a reactor model which might have separate effects. However, under the selected conditions only the primary reactions are active, so the same analysis is also presented using a reactor model. Note that those results are inherently different as they consider the selectivity towards ethane and ethylene, rather than only the formation of ethane. The partial pressures of methane and oxygen were varied in a way that corresponds to a C/O ratio varying between 0.5 and 30. As can be seen in figure 4.10a the C_2 selectivity does not monotonically increase with the C/O ratio. In fact, past a moderate C/O ratio, the selectivity only decreases. Furthermore, the same effect is seen in figure 4.10b using the reactor model.

However, it must not be concluded that this kinetic model is entirely invalid.

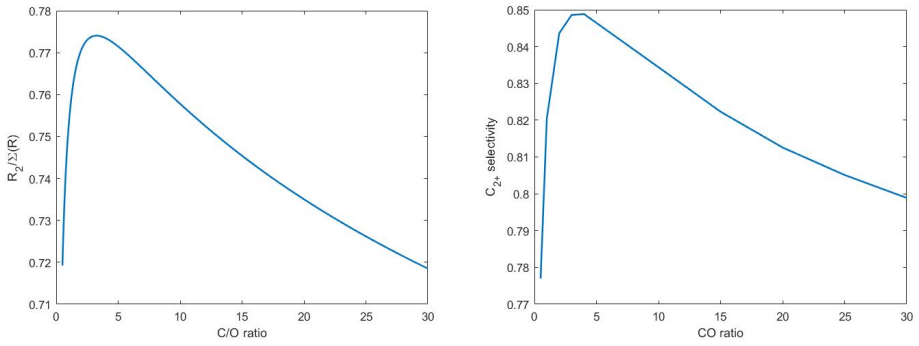

(a) Instantaneous selectivity

(b) Reactor model

Figure 4.10: C_2 selectivity evaluated as function of C/O ratio in two different ways. $T = 850°C$, Daneshpayeh kinetics.

Even at a C/O ratio of 30 the selectivity is not very low, and maybe not very far from what it should be. But the reactor model developed in this work often has C/O ratios in the hundreds near the membrane surface. This makes the results obtained with the Daneshpayeh kinetics in this work less valuable. For the sake of completeness, the Stansch kinetic is subjected to the same evaluation in figure 4.11. Clearly, the selectivity shows the expected behaviour, only increasing with increasing C/O ratio. Combined with the more successful distributed-feed validation (figure 4.8), this makes it interesting to also investigate the membrane reactor and fuel cell with the Stansch kinetics.

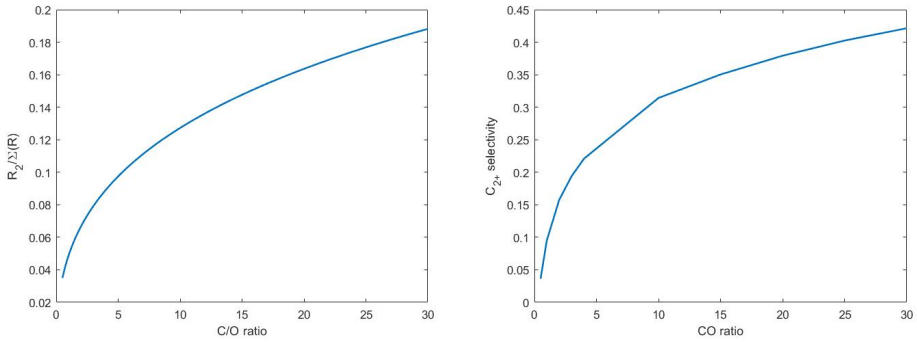

(a) Instantaneous selectivity

(b) Reactor model

Figure 4.11: C_2 selectivity evaluated as function of C/O ratio in two different ways. $T = 850°C$, Stansch kinetics.

5 Methods

In this section the definitions are discussed which are used to quantify the reactor performance both in terms of reactor engineering and additional quantities relevant to the fuel cells. Lastly, the methods related to the shortcut techno-economics are discussed.

5.1 Reactor performance

The conversion is the fraction of used reactant. The methane conversion X_{CH_4} is defined as follows:

$$X_{CH_4} = \frac{F_{CH_4,in} - F_{CH_4,out}}{F_{CH_4,in}} \tag{5.1}$$

F denotes the mole flow. In the case of OCM, the desired products contain two carbon atoms while all other carbon-containing species only have a single one. So, 10 moles of methane can yield 5 moles of ethylene at most. This leads to the definition for ethylene selectivity shown in equation 5.2 [9, 43].

$$S_{C_2H_4} = \frac{2F_{C_2H_4,out}}{2F_{C_2H_4,out} + 2F_{C_2H_6,out} + F_{CO,out} + F_{CO_2,out}} \tag{5.2}$$

Note that only the carbon-containing products are considered. If for example water were also considered, the above example would not result in 100% ethylene selectivity as converting 10 moles of methane to ethylene also results in 20 moles of water.
The product yield is defined as the product of reactant conversion and product selectivity.

$$Y_{C_2} = X_{CH_4} \cdot S_{C_2} \tag{5.3}$$

Another important metric for the analysis of OCM reactor behaviour is the C/O ratio: this is the ratio of methane to oxygen. In co-feeding, this refers to the inlet composition as long as full oxygen conversion is achieved. The C/O ratio for distributed-feeding is defined as the amount of fed methane in comparison to the amount of permeated oxygen, which can be calculated after the experiment or simulation has been completed. The C/O ratio is often an important cause of reactor performance. For example, at high C/O ratios there is relatively little oxygen available, and the reaction is expected to proceed more selectively than if the C/O ratio were lower.
Similarly, the C_2 ratio R_{C_2} is also an important metric for the evaluation of OCM: when this ratio is high, less ethane needs to be separated and dehydrogenated. Therefore a higher R_{C_2} indicates more favorable techno-economic prospects.

5.2 Fuel cell characteristics

In this thesis fuel cells are investigated, which produce power. The amount of power produced by a fuel cell is defined as in equation 5.4.

$$P_{cell} = V_{load} \cdot J \cdot 2\pi R L_R \tag{5.4}$$

Where J is the current density. The inner radius of the reactor R is used because the current density J has been defined with respect to the inner surface (the anode). Another important parameter to fuel cell operation is the fuel utilization. In this thesis it has been defined as shown in equation 5.5.

$$U_F = \frac{2F_{CH_4,in} + F_{H_2,in} - F_{H_2,out}}{2F_{CH_4,in} + F_{H_2,in}} \tag{5.5}$$

The fuel utilization is used as a measure the hydrogen utilization, which ultimately is the fuel for the electrochemical reaction. Since the majority of the hydrogen is not fed to the fuel cell but generated in situ, the amount of hydrogen which could be available from the reforming of methane (two H_2 molecules per molecule of CH_4) is taken into account.

5.3 Shortcut techno-economics

A short techno-economic analysis is presented which is just a comparison of operating expenses (OPEX) and the revenues of ethylene and electrical power. An estimation is presented which represents the OPEX which would be associated with operating an OCM plant at a total capacity of 135000 t/y of ethylene [7]. The correlation is shown in equation 5.6.

$$\text{OPEX} = \frac{43}{Y_{C_2H_4}} + \frac{299}{S_{C_2H_4}} - 136 \text{ €}/t \text{ ethylene} \tag{5.6}$$

In this correlation, OPEX contributions such as reactants, compressions, caustic wash, steam and refrigerant are included. Furthermore, a co-feeding reactor is

assumed, where the used oxygen is purchased through pipeline. The only considered reactions were methane combustion to CO_2 and direct reaction to ethylene. These assumptions are not a perfect match for the distributed-feed systems modeled in this thesis, but the correlation still gives an indication of what the operating expenses might be. The costs and prices related to ethylene and electrical power are given in table 5.1. The prices in table 5.1 are not from the same year as the cost

Table 5.1: Market prices used in this thesis. Source [46]

Ethylene	$P_{C_2} = 900$ €/t
Electricity	$P_E = 50$ €/kWh

correlation in equation 5.6, so the results obtained by comparing them will not be entirely accurate. A complete techno-economic analysis is beyond the scope of this work.

Aside from the OPEX, two other economic factors are considered: the ethylene revenue Q_{C_2}, and the electricity revenue Q_E. In order to reconcile all of these in units of €/t ethylene, the ethylene production rate of a single reactor C_{C_2} in units t ethylene/h is used. C_{C_2} is assumed equal to the sum of the ethylene and ethane flows leaving the reactor, as ethane dehydrogenation is assumed to be included in any OCM process scheme.

The electricity revenue in the integrated power case (OCM SOFC) is defined as the product of the cell power and the electricity price, divided by the ethylene capacity of the reactor, as shown in equation 5.7.

$$Q_E^{integrated} = P_{cell} \cdot P_E / C_{C_2} \tag{5.7}$$

In the case of the separated power case (OCM membrane reactor followed by reforming SOFC), it needs to be taken into account how the reactor effluent is divided over the necessary number of fuel cells. This is shown in equation 5.8.

$$Q_E^{separated} = \frac{F_{\text{post-sep}}}{F_{\text{SOFC-inlet}}} \cdot P_{cell} \cdot P_E / C_{C_2} \tag{5.8}$$

In equation 5.8, $F_{\text{post-sep}}$ refers to the mass flow rate of the effluent of a single OCM membrane reactor, after product separation. $F_{\text{SOFC-inlet}}$ refers to the mass flow rate at which the same mixture is introduced to the SOFC.

6 Results

In this section, the results are presented which have been obtained using the developed reactor model. Some results are first discussed which have been generated using the kinetic model of Daneshpayeh et al. The main body of results is presented thereafter, which concern simulations performed with the kinetic model of Stansch et al. Lastly, the shortcut techno-economic analysis is presented.

6.1 With Daneshpayeh kinetics

The results are built by successive comparison starting from a co-feed case. In order to establish this case, the results from the co-feed thermal validation case were used as a basis. A single adjustment was made to the validation case, namely that the residence time needed to be increased in order to obtain complete oxygen conversion.

6.1.1 Dilution in co-feed

The feed of the co-feed case described above is composed of a mixture with a ratio of CH_4:O_2:N_2 = 3:1:2.5. This means that it is operated under dilution. The first question which arises is whether that is necessary. A straightforward comparison which allows this question to be answered is with the same case, but with feed ratio CH_4:O_2:N_2 = 3:1:0. The comparison of the two cases is shown in table 6.1. As can be seen in table 6.1, the selectivity starkly decreases when dilution

Table 6.1: Co-feed comparison of diluted and undiluted reactor performance with Daneshpayeh kinetics. T = 750°C, p = 1 bar

Tube inlet composition	X_{CH_4}	S_{C_2}	Y_{C_2}	ΔT(°C)
CH_4:O_2:N_2 = 3:1:2.5	42%	70%	29%	33
CH_4:O_2:N_2 = 3:1:0	37%	42%	16%	98

is removed. Because of the lack of dilution, the partial pressures of the reactants are higher, and the reaction proceeds more rapidly as a consequence. This makes the temperature rise much more severe, while the temperature rise is only $33°C$ in the diluted case. In the model used in this thesis, the selectivity monotonically decreases with temperature, though that is not what is observed experimentally [42, 10]. This problem was also observed in section 4.2, and will be discussed in section 6.2.3. The decrease in methane conversion can also be explained given this decreased selectivity: oxygen is the limiting reactant, and the undesired reactions consume stoichiometrically more oxygen. Overall, the conclusion can be drawn that dilution can be an important measure to increase performance if a decrease in the temperature rise is desired. However, the model wrongly shows that the minimum temperature is the best.

6.1.2 Dilution in distributed-feed

It is interesting to carry out the same comparison of the role of dilution within distributed-feeding. In order to obtain these cases, oxygen was no longer co-fed, resulting in tube inlet compositions of CH_4:O_2:N_2 = 3:0:2.5 and CH_4:O_2:N_2 = 3:0:0. Instead, oxygen was introduced to the system by setting the boundary conditions with an oxygen flux equation corresponding to a BCFZ perovskite membrane (equation 2.2 in section 2.2). The residence time for each case is adjusted in order to obtain a C/O ratio equal to 3 at the outlet. The results are shown in table 6.2. Here, the opposite effect is seen as in co-feeding with regards to selectivity:

Table 6.2: Distributed-feed comparison of diluted and undiluted reactor performance with Daneshpayeh kinetics. T = 750(°C), p = 1 bar

Tube inlet composition	X_{CH_4}	S_{C_2}	Y_{C_2}	ΔT(°C)
CH_4:O_2:N_2 = 3:0:2.5	35%	34%	12%	<1
CH_4:O_2:N_2 = 3:0:0	40%	35%	14%	<1

the selectivity increased when dilution was removed. The first major contributor to this fact is the temperature rise, as it is limited to only half a degree Celsius in the undiluted case. It is of the same magnitude for the diluted case. This is curious, as OCM is known to also have significant temperature rises under distributed feeding of oxygen. But given that it is so, some other explanation for the selectivity change is needed when changing the dilution. In fact, the small selectivity change might be due to the dilution itself. Under dilution, the partial pressures of the reactants is decreased. The undesired reactions in general have lower reaction orders in the hydrocarbon reactants than the desired reactions, for which those reaction orders are around unity. Therefore the selectivity slightly decreases under dilution, but normally this will not be seen as the thermal effects of dilution on the selectivity are much greater.

6.1.3 Co- and distributed-feed comparison

However, the most important difference is to be seen between tables 6.1 and 6.2: The selectivity in distributed-feeding is lower than in co-feeding, which is not in agreement with experimental findings. This was also discussed in enough detail in section 4.4, where it was concluded that it is inherent to the kinetic parameters, and not the reactor model. This means that it is not interesting to discuss further results which were obtained using the Daneshpayeh kinetic model.

6.2 With Stansch kinetics

6.2.1 Establishing the co-feed case

The need has been expressed to establish a co-feed case. However, as shown in section 4.3.1, using the Stansch kinetic parameters as reported gave an unsatisfac-

tory result. This took the form of full oxygen conversion within an unreasonably short reactor length (a few mm), as well as a gross overestimation of the temperature rise. Both of these phenomena are caused by an overestimation of the overall reaction rate. Note that this problem did not occur in the distributed-feeding validation with the same kinetic model. In order to establish a co-feed case an artificial catalyst dilution is introduced, but it is not used for the distributed-feed simulations which will follow.
Two criteria were used to choose the artificial catalyst dilution: first of all, the oxygen conversion should reach completion within a reasonable reactor length of a few centimeters. This is considered reasonable based on the experimental results used for the co-feed validation study [43] (figure 4.5). This co-feed case is the same as the attempted thermal co-feed validation in section 4.3.1, except for the catalyst dilution factor. So the temperature rise should also be more reasonable, i.e. less than one hundred degrees Celsius. Using these criteria, an artificial catalyst dilution factor of 25 was chosen. This results in full oxygen conversion over roughly 3 cm of catalyst bed, and a temperature rise of 43 degrees Celsius.

6.2.2 Dilution in co- and distributed-feed

For the questions regarding dilution in both co- and distributed-feeding some of the same rationales apply as were discussed for the results obtained with the Daneshpayeh kinetic. Therefore, comparison of dilution effects and oxygen feeding policy are presented together in table 6.3.

As can be seen in table 6.3, the methane conversion achieved in the two co-

Table 6.3: Comparison of (un)diluted and co-/distributed-feeding reactor performance with Stansch kinetics. T = 750°C, p = 1 bar, C/O ratio 3

O_2 Feed policy	Tube inlet composition	X_{CH_4}	S_{C_2}	Y_{C_2}	ΔT(°C)
Co-feed	CH_4:O_2:N_2 = 3:1:2.5	29%	37%	11%	43
Co-feed	CH_4:O_2:N_2 = 3:1:0	27%	22%	6%	121
Distributed-feed	CH_4:O_2:N_2 = 3:0:2.5	39%	64%	25%	<1
Distributed-feed	CH_4:O_2:N_2 = 3:0:0	42%	70%	30%	<1

feeding cases is similar, but again the selectivity suffers from the increased temperature rise which takes place in absence of feed dilution. Also, the selectivity in these co-feed cases is lower than expected. Contrary to the co-feed cases, the temperature rise is insignificant in the case of distributed oxygen feed. The selectivity improves in the absence of dilution due to the reaction orders in the hydrocarbons (the same effect as is present in the kinetic model of Daneshpayeh). Also it must be mentioned that the length of the reactor was changed to 15 cm for the distributed-feed cases, in order to have an L/D ratio which was more reflective of experimental results. This has contributed to the limited extent of the temperature rise compared to the co-feeding cases. However, the temperature

rises in distributed-feeding are so minor that this cannot be the sole reason. But most importantly, distributed feeding has a high selectivity, as expected.

6.2.3 Temperature dependence

In section 6.1 it was mentioned that the simulated system exhibits a monotonic decrease in C_2 selectivity with increasing temperature. The question remains if this is not due to ill-chosen operating conditions. Distributed-feed simulations were

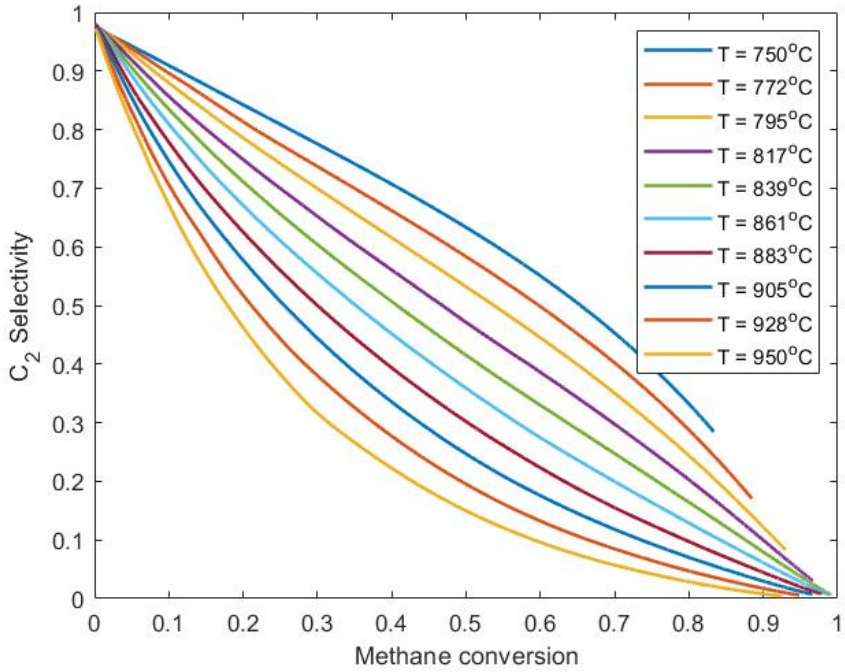

Figure 6.1: Distributed-feed C_2 selectivity at a wide range of methane conversion and temperature obtained with the Stansch kinetics

carried out, varying the temperature over the kinetic model's complete range of validity, in order to investigate the temperature-dependence of the C_2 selectivity. The result is shown in figure 6.1. In figure 6.1 it can be seen the selectivity decreases with temperature over the entire range of methane conversion. It must be mentioned that the C/O ratio changes with conversion (it decreases). For two points which are at equal conversion, the one with higher selectivity has a lower C/O ratio. Therefore, if the x-axis was changed to the C/O ratio, the selectivity lines would be more separated, and still in the same order.
This means that a selectivity maximum with temperature, as observed experimentally, will never be predicted by the used reactor model. It is unlikely that this is due to the kinetic model itself, because other authors have shown a selectivity maximum with temperature in a simulation using the Stansch kinetics [47, 48]. It

is more likely that it is due to an implementation error in the model used in this thesis.

6.2.4 Best membrane reactor case

In figure 6.1 it can be seen that the best selectivity is obtained at the lowest temperature. Based on this result, the best reactor performance will always be at the lowest temperature. The lowest temperature at which the Stansch kinetics are measured is 750°C, so no simulations are carried out below that temperature.
None of the cases presented in table 6.3 are the best possible. Development of the

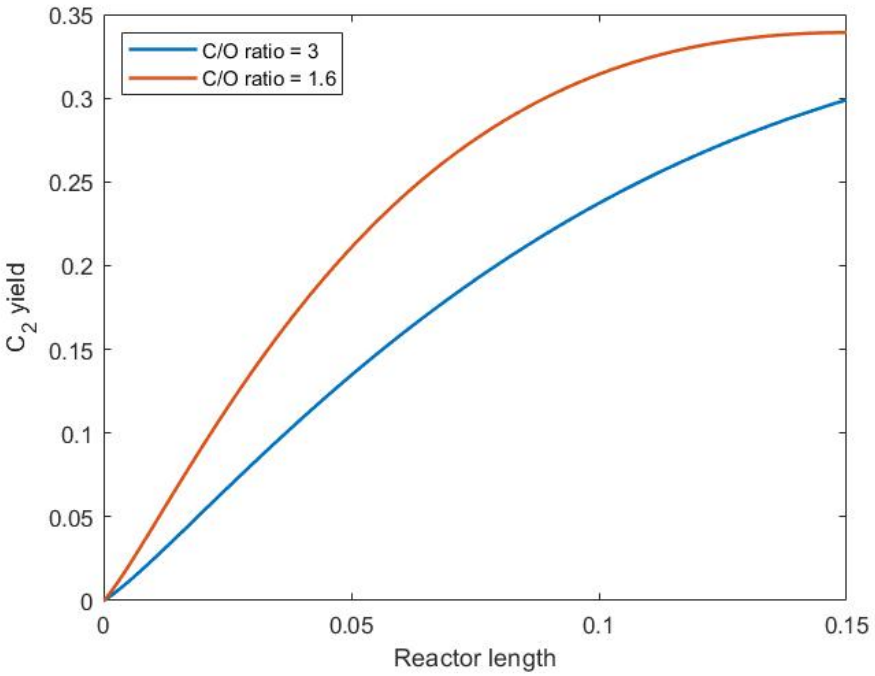

Figure 6.2: Adjustment of residence time to get the maximum yield in‘the undiluted distributed-feeding simulation. T = 750 ° C

best membrane reactor case obtained in this thesis is discussed below. Because of the reasons discussed previously, the temperature will be kept at 750°C. As can be seen in figure 6.2 the residence time could be increased in order to obtain a greater C_2 yield. The resulting C/O ratio is 1.6. The reactor performance of this case is given in table 6.4. This result is the best which has been obtained in the membrane reactor in this thesis, and is near the result of one of the best experimental efforts ($Y_{C_2} = 34.7\%$ [49]), which was also obtained under distributed feeding, albeit under different temperature and dilution.

Table 6.4: Best reactor performance of distributed-feed case. T = 750°C, p = 1 bar

C/O ratio	X_{CH_4}	S_{C_2}	Y_{C_2}
1.6	61%	55%	34%

6.2.5 OCM in SOFC

A SOFC was simulated in which OCM takes place in the anodic chamber. This is the same model as was used for the previous distributed-feed cases, except that the flux equation was changed from the equation governing BCFZ oxygen permeation to the electrochemical model. The power characteristic of the OCM SOFC is shown in figure 6.3. Note that this is plotted as power density (W/m^2) versus load voltage, while traditionally the power characteristic is plotted as power density versus current density. This method however is more congruent with the reactor performance analysis which will follow. As can be seen in figure 6.3, the system

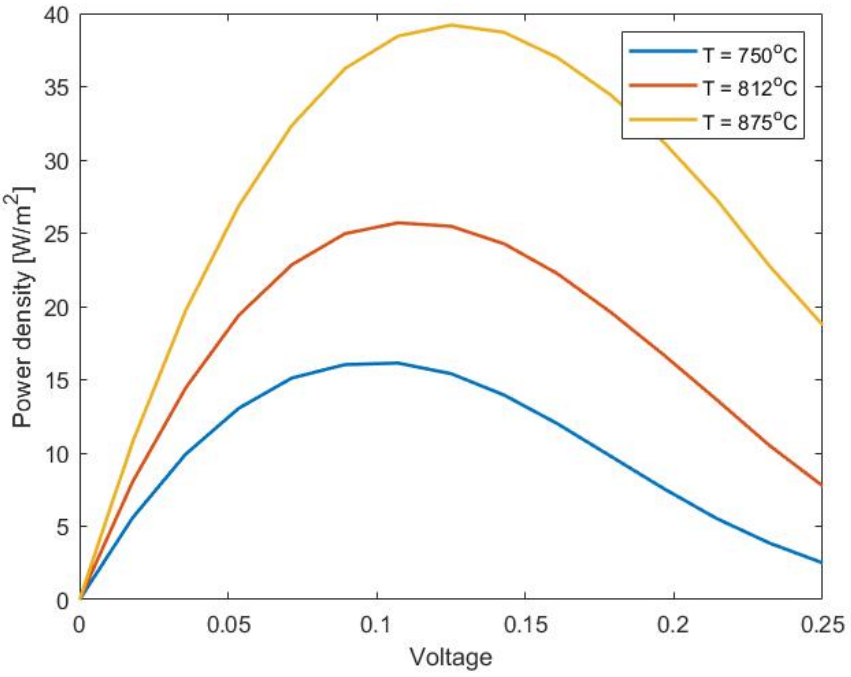

Figure 6.3: Power characteristic of the OCM SOFC at different temperatures

behaves fully as expected with higher temperatures leading to increased power generation. The thermodynamic effect of the absence of a ΔG_0 in the Nernst voltage related to the electrochemistry assumed here ($O_2 \rightarrow O_2$) is also clearly visible, as the maximum voltage is not much larger than the depicted 0.25 V, and consequently the power density is only of the order 10 W/m^2. In SOFCs with hydrogen,

power densities of the order 1000 W/m^2 are more common [27, 30]. The fact that a SOFC operated with OCM has such a low power density is also observed in other research [24, 25].
An analysis is presented of the effects of varying the load voltage of the fuel cell. The load voltage has implications for the reactor performance: an increased load voltage leads to a decreased current density and therefore decreased oxygen flux. Because of this, the reactor cannot necessarily be operated at a voltage which results in maximum power. The temperature is also varied: the SOFC generates more power at higher temperature, and the reaction rate is increased (which can be used to offset the decreased throughput due to decreased oxygen flux at higher voltages). The results which are presented at these varied values of operating temperature and load voltage are not presented at constant flow rate. Rather, for each combination of temperature and voltage there is a single flow rate which leads to maximum C_2 yield, and that still remains the most important goal. Furthermore, the electrochemical behaviour is only very weakly sensitive to the methane flow rate within the limits of incomplete methane conversion, which is always the case with OCM.
What can be seen in figure 6.5 is first and foremost that unrealistic yields are predicted at high voltage and 750 degrees Celsius. It can be explained that the model shows this behaviour: the oxygen flux is decreased at high voltage, which in turn leads to a lower partial pressure of oxygen. At extremely low partial pressures, a very high selectivity is predicted. This model behaviour is confirmed by the result shown in figure 6.4. There a perovskite membrane reactor was simulated, while changing the O_2 flux artificially by multiplying the flux with a constant factor ranging from 1/4 to 4. It is however not apparent from experimentation that low fluxes can result in such high yields. One reason might be that membrane reactors with such a low flux simply exhibited membrane instability in the form of coking. It is beyond the present work to say definitively what realistically is the maximum voltage with respect to coking or other experimental complications. Even if these results were obtainable experimentally, the voltage which corresponds to the highest yield also corresponds with a mass flow rate of methane which is roughly 20 times lower than that in the best membrane reactor case presented in section 6.2.4, and this is unfavorable from a techno-economic perspective.
Rather than investigating the highest yield, it is interesting to investigate whether the SOFC could be operated with performance and throughput similar to the best membrane reactor case, while also producing power. From figure 6.5, the minimum voltage can be identified at which the yield is at least as good as in the best membrane reactor case, and from figure 6.6 the maximum voltage can be identified below which the throughput remains better. At T = 875°C, the minimum voltage is larger than the maximum voltage, so such a region is not present. At T = 812°C, the same discrepancy is present, but it is much smaller: with a voltage of 0.1405 V, the fuel cell could achieve 34% yield with a mass flow rate equal to 97% of that in the best membrane reactor case. At this voltage and temperature, a current density of 24.44 W/m^2 is obtained. At T = 750°C, the voltage may vary

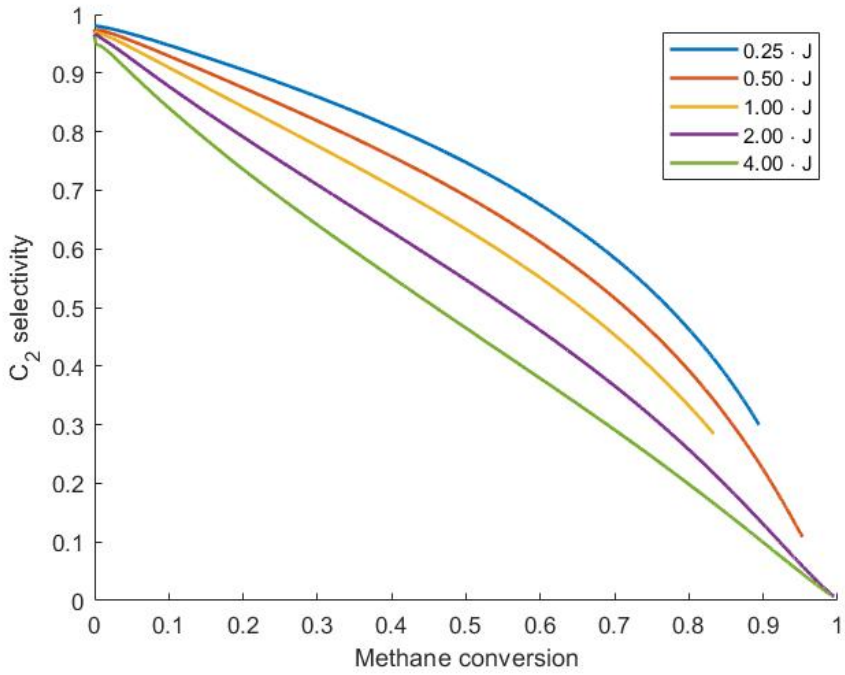

Figure 6.4: The effect of artificially varying the O_2 flux on selectivity in a distributed-feeding reactor, T = 750°C

between 0.0804 < V < 0.0840. This results in a yield just above $Y_{C_2} = 34\%$ at a minor expense to the flow rate (which is still 99.9% relative to the best membrane reactor case). These results are summarized in table 6.5. It is suspicious

Table 6.5: OCM SOFC performance and power generation

Temperature °C	Voltage	Power density	X_{CH_4}	S_{C_2}	Y_{C2}	Relative flow rate
750	0.0840	15.76	53%	65%	34%	99.9%
812	0.1405	24.44	53%	64%	34%	96.6%

that the SOFC can have the same reactor performance as the membrane reactor whilst also producing power. Therefore it must be noted that this is only possible because the fuel cell exhibits a higher flux at short circuit conditions ($V_{load} = 0$) than the perovskite membrane reactor. This fact in turn is based on the choice of cell design: the combined thickness of the anode, cathode and electrolyte was set equal to the thickness of the BCFZ membrane (0.5 mm). Apparently, it can be said that the materials used in the fuel cell exhibit a higher permeance than the perovskite. However, the material thickness would in reality be subject to material strength requirements, and using equal thicknesses might not be possible

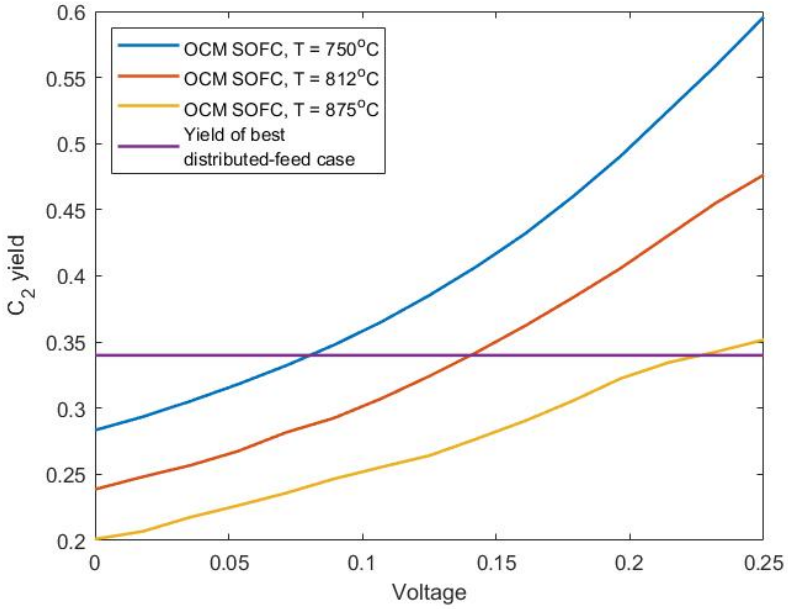

Figure 6.5: The C_2 yield as a function of load voltage in OCM SOFC. The yield of the best membrane reactor case is included for comparison

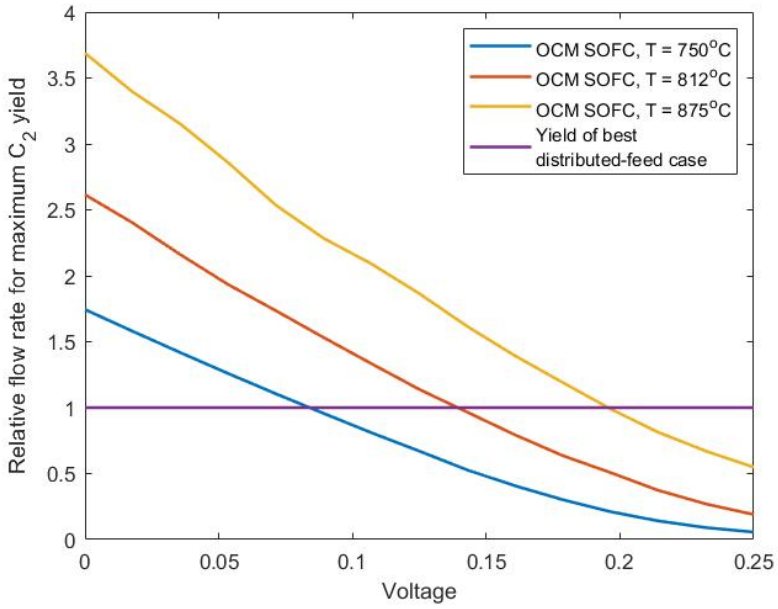

Figure 6.6: Mass flow rate relative to the flow of the best membrane reactor case, which is included for comparison

(without making one of the two thicker than it needs to be). Checking the reactor designs for mechanical strength is outside the scope of this thesis.

6.3 Internal reforming SOFC

The internal reforming SOFC is used to generate power using the effluent of the best membrane reactor case. The assumptions about separation of the products are described in section 5.3. The composition of the reactor effluent before and after applying those assumptions is shown in table 6.6. Using this composition,

Table 6.6: Composition (wt%) of the effluent of the best membrane reactor case, before and after separation assumptions

	CH_4	C_2H_6	C_2H_4	CO	CO_2	H_2	H_2O
Before separation	27.3%	4.1%	8.0%	3.2%	27.0%	1.1%	29%
After separation	46.7%	0%	0%	5.4%	46.1%	1.8%	0%

a flow rate was chosen at which a reasonable fuel utilization was had across the varying operating conditions. The power characteristic of the SOFC was generated by varying the load voltage. This was done at 750, 800, and 850 degrees Celsius because the reforming kinetics are based on experiments in that temperature range. As can be seen in figure 6.7, power densities of the order 1000 W/m^2 are obtained, which is generally expected for SOFCs [27]. The maximum power density was obtained at a load voltage of $V_{load} = 0.6857$ V (for all three temperatures). As the power generation clearly increases with temperature (as expected), the temperature of 850°C is the most promising.
However, the data point in figure 6.7 which corresponds to the maximum power density had a fuel utilization of only 30%. In order to obtain the maximum power generation from the available feed, the fuel utilization was increased as much as possible (76%) by increasing the residence time in the reforming SOFC. Higher fuel utilization was attempted, but was not achieved due to failure of the ODE solver to reach the full reactor length. This modification to the residence time resulted in a ratio $F_{post-sep}/F_{SOFC-inlet}$ of 5.29, meaning that the post-separation effluent of 5.29 OCM reactors is needed to feed a single fuel cell. The total power generation increased by roughly 30%. A summary of the performance of the reforming SOFC is shown in table 6.7. Practically full methane conversion is

Table 6.7: Performance summary of the internal reforming SOFC

T (°C)	P_{max} (W/m^2)	U_F	X_{CH_4}
850	1628.3	76%	99.9%

achieved within the reforming SOFC, which is unusual given that the reforming reactions are subject to equilibria. It should however be noted that the electrochemical reaction continually shifts the equilibrium towards the product side by

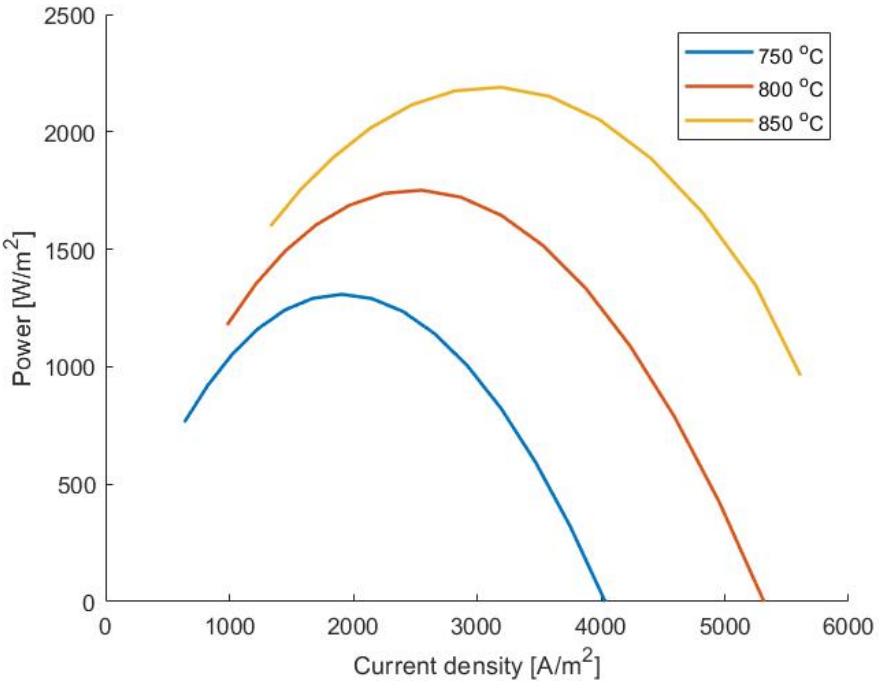

Figure 6.7: The power characteristic of an internal reforming SOFC using a dry feed

converting hydrogen to water. In order to have any certainty about the validity of this behaviour, a validation study should be carried out for the reforming reactor model.

6.4 Shortcut techno-economic estimation

Three cases have been developed where a well-performing OCM reactor is combined with power generation. Two of them concern the result which is obtained when both OCM and power generation are integrated within a single SOFC reactor, but at two different temperatures. In the last case, OCM and power generation are separated into two separate units. In this way, OCM and power generation can be done at different operating conditions. In table 6.8 a summary is given of the respective reactor performances and power generation associated with the three cases described above. The combined selectivity and yield of ethane and ethylene is not reported, but only the selectivity and yield towards ethylene: this is because the latter is used in the correlation with which the OPEX are estimated (equation 5.6). Using the information in table 6.8 as well as the flow rates which resulted from the reactor simulations, the expenses and revenues were calculated. The results are given in table 6.9. When looking at the information in table 6.9, it is clear that the separated power generation case is the most economical. However,

Table 6.8: Summary of reactor performance and power generation of the three developed cases

Case	X_{CH_4}	$S_{C_2H_4}$	$Y_{C_2H_4}$	R_{C_2}	P_{cell} (W/m^2)	T (°C)
Integrated(1)	53%	42%	22%	1.80	15.76	750
Integrated(2)	53%	49%	26%	3.83	24.44	812
Separated	61%	37%	23%	2.01	1628.3	750*/850**

*Reactor temperature; **SOFC temperature

Table 6.9: Results of techno-economic calculations. All figures in units €/t ethylene

Case	OPEX (€/t)	Q_{C_2} (€/t)	Q_E (€/t)	Net revenue (€/t)
Integrated(1)	774	900	23	149
Integrated(2)	648	900	36	288
Separated	863	900	409	445

it must be noted that its net revenue is almost completely composed out of the power generation revenue. Regarding the OPEX and ethylene yield, the separated case is actually the worst. Interestingly, the first integrated case and the separated case have similar ethylene yield, but different OPEX. The OPEX correlation shows that high ethylene selectivity is more important to have than high methane conversion. This is in agreement with other, much more detailed techno-economic analyses [5, 4]. The higher ethylene selectivity observed for the second integrated power generation case coincides with a higher ratio of ethylene to ethane. This ratio is known to increase with temperature. A higher C_2 ratio is beneficial to the OCM process economics. The incorrect temperature dependency of the OCM selectivity (discussed in section 6.2.3) is therefore extra problematic, as the highest yields of ethylene and ethane predicted by this model now coincide with low C_2 ratios. Of course, this can be remedied by combining the internal reforming SOFC with another OCM reactor case, due to its independent nature. Therefore, the separated power generation case can be considered better than the integrated one.

It must be noted that the OPEX is estimated with less accuracy for the separated power generation case than for the integrated cases. This is because the addition of the reforming reactor completely changes the separation train. Also, the reforming reaction presents an opportunity for heat integration with OCM which is not reflected in the presented results.

For both integrated cases, the electricity revenue is not very significant. Integrated energy production will only be interesting if the fuel cell technology is not significantly more expensive than the relatively simpler membrane reactors, but even then it would make more sense to dedicate SOFCs solely to power generation.

The low economic benefit of doing OCM in SOFC has another more positive implication: If only a small revenue is gotten from fuel cells, then maybe electrolyzers could be employed with low cost. Solid-oxide electrolyzers can be used to obtain an increased oxygen flux, at the expense of electrical power. Whether or not this approach would be beneficial can however not be said based on these results, and other research has to be consulted.

7 Conclusion and Discussion

A 2D reactor model was developed in order to describe radial profiles with both mass and heat balances. With the Daneshpayeh kinetics, realistic thermal behaviour of OCM co-feeding was simulated in co-feeding. Reactor performance was predicted up to an acceptable level of accuracy: the remaining error was probably due to the lack of gas-phase reactions in the kinetic model. Though this seemed promising, it has been shown that the Daneshpayeh kinetic model does not predict the selectivity increase expected under distributed feeding. Fortunately, this selectivity trend was correctly predicted using the Stansch kinetics. However, it has been implemented with some error in this thesis, leading to an incorrect temperature dependence for the selectivity: selectivity was found to decrease with temperature, while this is not observed in experiments or other modelling efforts using the same kinetic model. Not only was the thermal dependence not correctly modeled, but the thermal behaviour in distributed feeding is also suspicious: the temperature rise remained limited to a few degrees or even less.

Still, the Stansch kinetic model was used to investigate the operation for a membrane reactor and a SOFC reactor. It was found to be possible to have up to 34% yield in both reactor types, which is representative of the best experimental efforts. In fact, even much higher yields were predicted in the OCM SOFC model under increased load voltage. It is suggested that the model may lose its validity at higher load voltage, because the severely reduced oxygen flux would allow coking to take place. The results at relatively lower voltages are considered to have fluxes comparable to those in the membrane reactor, and are still considered valid.

Power generation in SOFC was investigated in two cases: with OCM in the anodic chamber, and with reforming. In the former case, there is no proper electrochemical reaction to be energetically favored, and the resulting power generation was very low. On the contrary, the internal reforming fuel cell resulted in the expected power production. It was noted that the methane conversion in the reforming SOFC was extremely high, and a kinetic validation study is necessary. A shortcut techno-economic analysis was presented, showing that power production with internal reforming SOFC can have a great benefit. The same benefit is not obtained with an OCM reactor SOFC.

Due to the thermal problems with the OCM kinetics, the 'separated' case where an OCM membrane reactor was coupled with an internal reforming SOFC was not the best when purely regarding the OCM performance. Specifically, the low temperature at which the model exhibited the highest C_2 selectivity, resulted in a relatively low C_2 ratio, and higher OPEX than was predicted with the OCM SOFC 'integrated' case. Of course, the reforming SOFC can be coupled with an OCM reactor which has better performance due to its independent nature, so it can still be said that the separated power generation case is superior.

8 Outlook

In order to improve the results which have been put forward in this thesis, it is paramount that the Stansch kinetics are implemented correctly. With that, a realistic estimation of the reactor behaviour could be presented. It would also be interesting to investigate OCM kinetics which include the effects of gas-phase reactions.
A validation of the reforming reaction would serve to further increase the confidence in the obtained results.
Performing OCM in a solid oxide electrolyzer could be economically interesting. How much energy is needed to obtain a significant increase in the oxygen flux can be investigated, as well as the economic consequences.
It would be interesting to reformulate the entire model as a root finding problem or to extend it with the shooting method. This would allow for the description of Ohmic heat generation and the counter-current nature of a closed-cap fuel cell.
Lastly, a completely new addition to the research is suggested. OCM can be combined with water splitting in the presence of certain perovskites [50]. Not only does this have the benefits of distributed feeding of oxygen, but also thermal integration with endothermic water splitting, and added hydrogen production. However, it still faces its own problems.

References

[1] T. Swift and M. Moore. "Shale Gas and New Petrochemicals Investment". In: *Changing Roles of Industry, Government and Research, 30th USAEE/IAEE North American Conference, Oct 9-12, 2011.* International Association for Energy Economics. 2011.

[2] P. Thiruvenkataswamy, F. T. Eljack, N. Roy, M. S. Mannan, and M. M. El-Halwagi. "Safety and techno-economic analysis of ethylene technologies". In: *Journal of Loss Prevention in the Process Industries* 39 (2016), pp. 74–84.

[3] A. Galadima and O. Muraza. "Revisiting the oxidative coupling of methane to ethylene in the golden period of shale gas: A review". In: *Journal of Industrial and Engineering Chemistry* 37 (2016), pp. 1–13.

[4] B. L. Farrell, V. O. Igenegbai, and S. Linic. "A viewpoint on direct methane conversion to ethane and ethylene using oxidative coupling on solid catalysts". In: (2016).

[5] J. C. W. Kuo, C. T. Kresge, and R. E. Palermo. "Evaluation of direct methane conversion to higher hydrocarbons and oxygenates". In: *Catalysis today* 4.3-4 (1989), pp. 463–470.

[6] A. Cruellas, J. Bakker, M. van Sint Annaland, J. Medrano, and F. Gallucci. "Techno-economic analysis of oxidative coupling of methane: Current state of the art and future perspectives". In: *Energy Conversion and Management* 198 (2019), p. 111789.

[7] X. S. Nghiem. "Ethylene Production by Oxidative Coupling of Methane: New Process Flow Diagram Based on Adsorptive Separation". Technischen Universität Berlin, 2014.

[8] A. Cruellas, T. Melchiori, F. Gallucci, and M. van Sint Annaland. "Advanced reactor concepts for oxidative coupling of methane". In: *Catalysis Reviews : Science and Engineering* 59(3) (2017), pp. 234–294.

[9] N. Holst, S. Jašo, H. R. Godini, S. Gloeser, H. Arellano-Garcia, G. Wozny, and J. Steinbach. "Two-Dimensional Model for Oxidative Coupling of Methane in a Packed-Bed Membrane Reactor". In: *Chemical engineering & technology* 35.2 (2012), pp. 294–301.

[10] Z. Stansch, L. Mleczko, and M. Baerns. "Comprehensive Kinetics of Oxidative Coupling of Methane over the La2O3/CaO Catalyst". In: *Industrial and Engineering Chemistry Research* 36 (1997), pp. 2568–2579.

[11] M. Daneshpayeh, A. Khodadadi, N. Mostouf, Y. Mortazavi, R. Sotudeh-Gharebagh, and A. Talebizadeh. "Kinetic modeling of oxidative coupling of methane over Mn/Na2WO4/SiO2 catalyst". In: *Fuel Processing Technology* 90 (2009), pp. 403–410.

[12] Y. Patcharavorachot, S. Tiraset, W. Wiyaratn, S. Assabumrungrat, and A. Arpornwichanop. "Using a membrane reactor for the oxidative coupling of methane: simulation and optimization". In: *Clean Technologies and Environmental Policy* 16 (2014), pp. 1295–1306.

[13] M. Daneshpayeh, N. Mostouf, A. Khodadadi, R. Sotudeh-Gharebagh, and Y. Mortazavi. "Modeling of Stagewise Feeding in Fluidized Bed Reactor of Oxidative Coupling of Methane". In: *Energy and Fuels* 23 (2009), pp. 3745–3752.

[14] S. M. K. Shahri and S. M. Alavi. "Kinetic studies of the oxidative coupling of methane over the $Mn/Na_2WO_4/SiO_2$ catalyst". In: *Journal of Natural Gas Chemistry* 18.1 (2009), pp. 25–34.

[15] A. A. Plazaola, A. Cruellas, Y. Liu, N. B. Porras, D. A. P. Tanaka, M. van Sint Annaland, and F. Gallucci. "Mixed ionic-electronic conducting membranes (MIEC) for their application in membrane reactors: a review". In: *Processes* 7.3 (2019), p. 128.

[16] A. J. Burggraaf and L. Cot. *Fundamentals of inorganic membrane science and technology*. (Book) Elsevier, 1996.

[17] C. S. Chen, H. Kruidhof, H. J. M. Bouwmeester, H. Verweij, and A. J. Burggraaf. "Thickness dependence of oxygen permeation through erbiastabilized bismuth oxide-silver composites". In: *Solid State Ionics* 99.3-4 (1997), pp. 215–219.

[18] S. J. Xu and W. J. Thomson. "Oxygen permeation rates through ion-conducting perovskite membranes". In: *Chemical Engineering Science* 54.17 (1999), pp. 3839–3850.

[19] O. Czuprat, T. Schiestel, H. Voss, and J. Caro. "Oxidative coupling of methane in a BCFZ perovskite hollow fiber membrane reactor". In: *Industrial & engineering chemistry research* 49.21 (2010), pp. 10230–10236.

[20] N. Lu, F. Gallucci, T. Melchiori, D. Xie, and M. van Sint Annaland. "Modeling of autothermal reforming of methane in a fluidized bed reactor with perovskite membranes". In: *Chemical Engineering and Processing-Process Intensification* 124 (2018), pp. 308–318.

[21] T. Nishino, H. Iwai, and K. Suzuki. "Comprehensive Numerical Modeling and Analysis of a Cell-Based Indirect Internal Reforming Tubular SOFC". In: *Journal of Fuel Cell Science and Technology* 3.1 (Feb. 2006), pp. 33–44.

[22] H. Worraphon, W. Wiyaratn, S. Assabumrungrat, and N. Laosiripojana. "Reactivity of Au/La1-xSrxCr1-yNiyO3-δ toward oxidative coupling of methane for C2 and C3 hydrocarbons production". In: *Engineering Journal* 18.4 (2014), pp. 1–12.

[23] A. V. da Rosa. *Fundamentals of renewable energy processes*. (Book) Academic Press, 2009.

[24] K. Liu, J. Zhao, D. Zhu, F. Meng, F. Kong, and Y. Tang. "Oxidative coupling of methane in solid oxide fuel cell tubular membrane reactor with high ethylene yield". In: *Catalysis Communications* 96 (2017), pp. 23–27.

[25] G. Xui-Mei, K. Hidajat, and C.-B. Ching. "Simulation of a solid oxide fuel cell for oxidative coupling of methane". In: *Catalysis today* 50.1 (1999), pp. 109–116.

[26] Y. Zhang, Y. Chen, and M. Yan. "An open circuit voltage equation enabling separation of cathode and anode polarization resistances of ceria electrolyte based solid oxide fuel cells". In: *Journal of Power Sources* 357 (2017), pp. 173–178.

[27] R. Bove and S. Ubertini. *Modeling solid oxide fuel cells: methods, procedures and techniques*. (Book) Springer Science & Business Media, 2008.

[28] T. R. Kuphaldt. *Lessons In Electric Circuits*. Fifth Edition. Vol. I–DC. (Book) Open Book Project, 2006.

[29] N. F. Bessette, W. J. Wepfer, and J. Winnick. "A mathematical model of a solid oxide fuel cell". In: *Journal of the Electrochemical Society* 142.11 (1995), p. 3792.

[30] P. Costamagna, A. Selimovic, M. Del Borghi, and G. Agnew. "Electrochemical model of the integrated planar solid oxide fuel cell (IP-SOFC)". In: *Chemical Engineering Journal* 102.1 (2004), pp. 61–69.

[31] D. Sánchez, R. Chacartegui, A. Munoz, and T. Sánchez. "Thermal and electrochemical model of internal reforming solid oxide fuel cells with tubular geometry". In: *Journal of Power Sources* 160.2 (2006), pp. 1074–1087.

[32] P. Costamagna and K. Honegger. "Modeling of solid oxide heat exchanger integrated stacks and simulation at high fuel utilization". In: *Journal of the Electrochemical Society* 145.11 (1998), p. 3995.

[33] H. J. Jun, M.-J. Park, S.-C. Baek, J. W. Bae, K.-S. Ha, and K.-W. Jun. "Kinetics modeling for the mixed reforming of methane over Ni-CeO2/MgAl2O4 catalyst". In: *Journal of natural gas chemistry* 20.1 (2011), pp. 9–17.

[34] M. Halabi, M. De Croon, J. Van Der Schaaf, P. Cobden, and J. Schouten. "Reactor modeling of sorption-enhanced autothermal reforming of methane. Part I: Performance study of hydrotalcite and lithium zirconate-based processes". In: *Chemical engineering journal* 168.2 (2011), pp. 872–882.

[35] U. Olsbye, T. Wurzel, and L. Mleczko. "Kinetic and reaction engineering studies of dry reforming of methane over a Ni/La/Al2O3 catalyst". In: *Industrial & engineering chemistry research* 36.12 (1997), pp. 5180–5188.

[36] H. P. Langtangen and S. Linge. *Finite difference methods for diffusion processes*. (Book) Simula research laboratory, 2016.

[37] G. W. Koning. “Heat and Mass Transport in Tubular Packed Bed Reactors at Reacting and Non-Reacting Conditions. Experiments and models”. Twente University, 2002.

[38] V. Specchia, G. Baldi, and S. Dicardi. “Heat transfer in packed bed reactors with on phase flow”. In: *Chemical Engineering Communications* 4.1-3 (1980), pp. 361–380.

[39] R. Bauer and E. U. Schlunder. “Effective radial thermal-conductivity of packings in gas-flow”. In: *International Chemical Engineering* 18.2 (1978), pp. 189–204.

[40] T. Gao and B. P. Jelle. “Thermal conductivity of amorphous silica nanoparticles”. In: *Journal of Nanoparticle Research* 21.18 (2019), pp. 1–6.

[41] S. Ergun. “Fluid flow through packed columns”. In: *Chem. Eng. Prog.* 48 (1952), pp. 89–94.

[42] A. Aseem and M. P. Harold. “C_2 yield enhancement during oxidative coupling of methane in a nonpermselective porous membrane reactor”. In: *Chemical Engineering Science* 175 (2018), pp. 199–207.

[43] A. Aseem, G. G. Jeba, M. T. Conato, J. D. Rimer, and M. P. Harold. “Oxidative coupling of methane over mixed metal oxide catalysts: Steady state multiplicity and catalyst durability”. In: *Chemical Engineering Journal* 331 (2018), pp. 132–143.

[44] T. Schiestel, M. Kilgus, S. Peter, K. Caspary, H. Wang, and J. Caro. “Hollow fibre perovskite membranes for oxygen separation”. In: *Journal of Membrane Science* 258.1-2 (2005), pp. 1–4.

[45] D. Kunii and O. Levenspiel. *Fluidization engineering*. (Book) Butterworth-Heinemann, 2013.

[46] H. R. Godini, M. Azadi, M. Khadivi, R. Schomäcker, F. Gallucci, G. Wozny, and J.-U. Repke. “Multi-Scale Analysis of Integrated C1 (CH4 and CO2) Utilization Catalytic Processes: Impacts of Catalysts Characteristics up to Industrial-Scale Process Flowsheeting, Part II: Techno-Economic Analysis of Integrated C1 Utilization Process Scenarios”. In: *Catalysts* 10.5 (2020), p. 488.

[47] Z. Zhang and S. Ji. “Numerical simulation of particle/monolithic two-stage catalyst bed reactor with beds-interspace distributed dioxygen feeding for oxidative coupling of methane”. In: *Computers & Chemical Engineering* 90 (2016), pp. 247–259.

[48] T. Eppinger, G. Wehinger, and M. Kraume. “Parameter optimization for the oxidative coupling of methane in a fixed bed reactor by combination of response surface methodology and computational fluid dynamics”. In: *Chemical Engineering Research and Design* 92.9 (2014), pp. 1693–1703.

[49] S. Bhatia, C. Y. Thien, and A. R. Mohamed. "Oxidative coupling of methane (OCM) in a catalytic membrane reactor and comparison of its performance with other catalytic reactors". In: *Chemical engineering journal* 148.2-3 (2009), pp. 525–532.

[50] Z. Cao, H. Jiang, H. Luo, S. Baumann, W. A. Meulenberg, H. Voss, and J. Caro. "Simultaneous overcome of the equilibrium limitations in BSCF oxygen-permeable membrane reactors: Water splitting and methane coupling". In: *Catalysis today* 193.1 (2012), pp. 2–7.